

1 **Multi-Machine Learning Ensemble Regionalization of Hydrological**
2 **Parameters for Enhancing Flood Prediction in Ungauged**
3 **Mountainous Catchments**

4
5 Kai Li, Linmao Guo, Genxu Wang*, Jihui Gao*, Xiangyang Sun, Peng Huang,
6 Jinlong Li, Jiapei Ma, Xinyu Zhang

7
8 *State Key Laboratory of Hydraulics and Mountain River Engineering, College of Water Resource
9 and Hydropower, Sichuan University, Chengdu, 610000, China*

10 *Corresponding author: Genxu Wang (wanggx@scu.edu.cn) and Jihui Gao (jgao@scu.edu.cn).

11

12 **Abstract:**

13 Machine learning-based parameter regionalization is an important method for
14 flood prediction in ungauged mountainous catchments. However, single machine
15 learning parameter regionalization often exhibits limitations in prediction accuracy and
16 robustness. Therefore, this study proposes a multi-machine learning ensemble
17 regionalization method that integrates Gradient Boosting Machine (GBM), K-Nearest
18 Neighbors (KNN), and Extremely Randomized Trees (ERT) methods (GBM-KNN-
19 ERT) to regionalize the sensitive parameters of the Topography-Based Subsurface
20 Storm Flow (Top-SSF) model. Validated across 80 mountainous catchments in
21 southwestern China, the GBM-KNN-ERT method demonstrates superior performance
22 with 90% of ungauged catchments achieving the Nash-Sutcliffe Efficiency (NSE)
23 above 0.9, representing a 67.44% improvement over the best single machine learning
24 parameter regionalization. Notably, the GBM-KNN-ERT method shows improved
25 robustness to climate change and changes in the number of donor catchments compared
26 to other regionalization methods. An optimal balance between accuracy and

27 computational efficiency was achieved using 20-40 high quality donor catchments
28 (NSE greater than 0.85). This study provides systematic evidence that multi-machine
29 learning ensemble can effectively address regionalization challenges in ungauged
30 mountainous regions, offering a reliable tool for water resource management and flood
31 disaster mitigation.

32 **Keywords:** Flood forecasting; Regionalization; Ungauged mountainous catchments;
33 Top-SSF model;

34

35 **Highlights:**

36 1. Proposes a novel multi-machine learning ensemble regionalization method
37 2. The GBM-KNN-ERT method increases the percentage of catchments with high-
38 accuracy flood predictions (NSE >0.9) to 90%, which is a 67.44% improvement
39 over the best single ML method.
40 3. The GBM-KNN-ERT method exhibits greater stability under climate change.

41

42 **1. Introduction**

43 Floods in mountainous catchments, encompassing both flash floods and general
44 larger-scale flood events which can be derived from mountainous upland catchments,
45 pose a significant threat to human safety and property, particularly in regions lacking
46 sufficient observational data (Luo et al., 2015; Zhai et al., 2018). While hydrological
47 models like the Topography-Based Subsurface Storm Flow (Top-SSF) model (Li et al.,
48 2024) offer promising simulation capabilities, their application in ungauged catchments
49 is severely limited by the absence of calibration data (Choi et al., 2023; Liu et al., 2018).
50 Effective parameter regionalization methods are therefore essential for transferring
51 hydrological knowledge from gauged to ungauged regions, enabling reliable flood
52 prediction in ungauged mountainous catchment (Garambois et al., 2015; Ragettli et al.,
53 2017; Xu et al., 2018).

54 Parameter regionalization is a crucial method for flood prediction in ungauged
55 catchments (Arsenault et al., 2022; Guo et al., 2021; Kratzert et al., 2019; Zhang et al.,
56 2020). Compared to purely data-driven methods, parameter regionalization offers
57 enhanced physical interpretability (Nearing et al., 2024; Tang et al., 2023; Zhang et al.,
58 2024). Existing parameter regionalization methods can be broadly classified into three
59 categories: similarity-based, hydrological signatures-based, and regression-based
60 (Arsenault et al., 2019; Wu et al., 2022). Similarity-based methods rely on the
61 assumption that catchments with similar characteristics exhibit similar hydrological
62 responses, considering spatial proximity (Arsenault et al., 2019; Pugliese et al., 2018;
63 Yang et al., 2018) and physical similarity (similar climatic and land cover conditions

64 have similar hydrological characteristics) (Kanishka et al., 2017; Papageorgaki et al.,
65 2016). Hydrological signature-based methods use hydrological signatures (quantitative
66 metrics that describe statistical or dynamic properties of streamflow) as an intermediate
67 link, establishing relationships first between model parameters and signatures, and then
68 between signatures and catchment descriptors to facilitate parameter transfer
69 (McMillan, 2021; Zhang et al., 2018). Regression-based methods, which directly link
70 hydrological model parameters to catchment descriptors, are widely used due to their
71 simplicity and computational efficiency (Guo et al., 2021; Kratzert et al., 2019; Song et
72 al., 2022; Wu et al., 2022). However, the performance of regression-based methods is
73 frequently constrained by the inherent nonlinearity in the relationships between model
74 parameters and catchment descriptors, coupled with the difficulty in adequately
75 capturing spatial heterogeneity, especially within complex mountainous terrain (Wu et
76 al., 2022).

77 Recent advances in machine learning offer potential solutions by capturing
78 nonlinear patterns in high-dimensional data. Such as Decision Tree (DT), Extremely
79 Randomized Trees (ERT), Gradient Boosting Machine (GBM), K-Nearest Neighbor
80 (KNN), Random Forest (RF), and Support Vector Machines (SVM) have shown
81 promise in parameter regionalization (Golian et al., 2021; Song et al., 2022). However,
82 existing machine learning-based parameter regionalization studies predominantly focus
83 on runoff prediction at coarser temporal scales (daily or monthly) (Li et al., 2022; Wu
84 et al., 2022), leaving a significant gap in high-resolution (hourly or sub-hourly) flood
85 prediction in ungauged mountainous catchments. Moreover, these studies often rely on

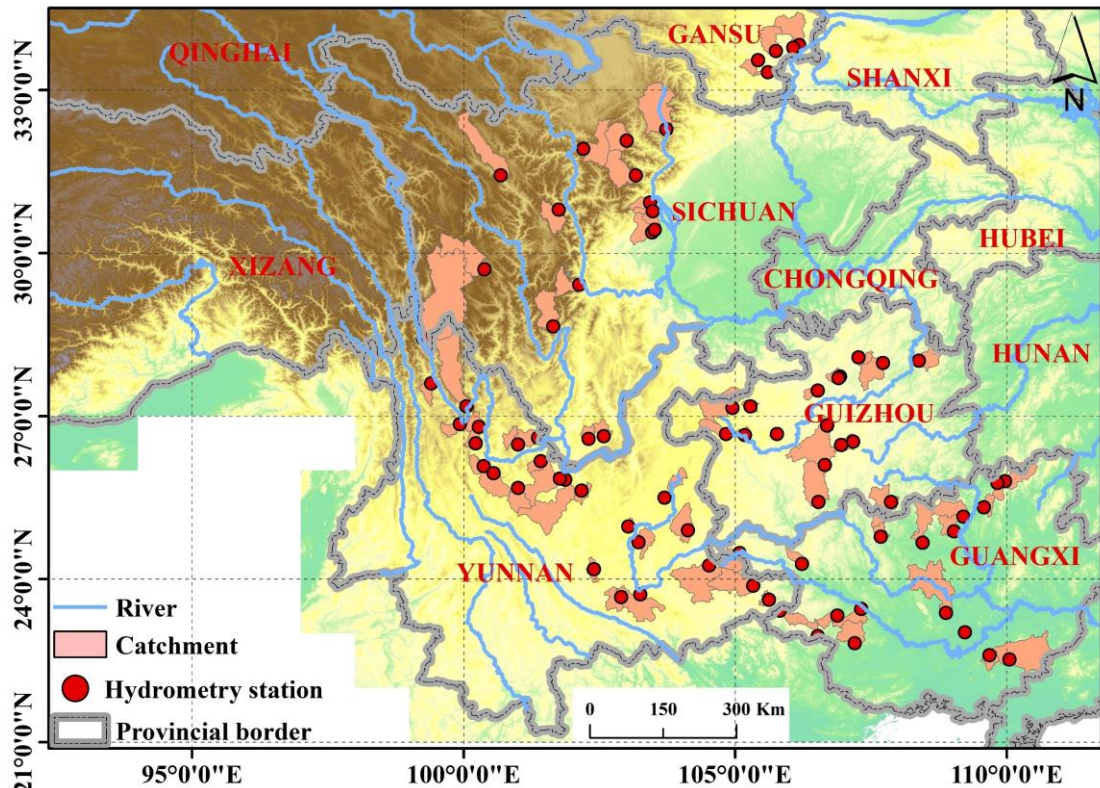
86 single machine learning methods to estimate all hydrological model parameters (Golian
87 et al., 2021; Song et al., 2022; Wu et al., 2022). Given that different machine learning
88 methods operate on distinct principles (Jordan et al., 2015; Zounemat-Kermani et al.,
89 2021) and hydrological model parameters represent diverse hydrological processes (Li
90 et al., 2024), a single machine learning method may not adequately capture the
91 complexity of model parameter estimation (Golian et al., 2021; Wu et al., 2022).
92 Therefore, exploring the multi-machine learning ensemble methods is essential to
93 improve the accuracy of high-resolution flood prediction in ungauged mountainous
94 catchments.

95 Southwest China's mountainous regions are particularly vulnerable to frequent
96 floods, leading to ecosystem degradation through habitat disruption and biodiversity
97 loss (Gan et al., 2018). The abundance of ungauged catchments in this region poses a
98 significant challenge to reliable flood prediction. To address this critical issue, we
99 systematically evaluate the performance of a novel multi-machine learning ensemble
100 method for regionalizing Top-SSF model parameters across 80 representative
101 catchments (mean area: 1,586 km²) in Southwest China. By assessing ensemble method
102 robustness under climate change and with varying donor catchment configurations, this
103 study aims to significantly enhance flood prediction accuracy in ungauged mountainous
104 catchments, contributing to improved ecosystem resilience, enhanced human safety,
105 and more effective water resource management in the face of escalating climatic
106 pressures.

107 **2. Study area and datasets**

108 **2.1. Study area**

109 This study investigated 80 mountainous catchments in Southwestern China,
110 encompassing Sichuan, Yunnan, Guangxi, Guizhou, and Chongqing provinces (Fig. 1).
111 This region exhibits diverse climatic zones, including subtropical monsoon, plateau
112 mountain, and tropical monsoon climates. The selected catchments have an average
113 area of 1,586 km² (ranging from 109 to 6,564 km²), with elevations ranging from 63 to
114 6,284 meters. Mean annual temperature varies from 15 to 20°C, and annual
115 precipitation ranges from 1,200 to 1,800 mm (Li et al., 2016), with approximately 80%
116 of the annual precipitation occurring during summer and autumn, contributing to
117 frequent flooding events (Cheng et al., 2019). These catchments are situated within a
118 heavily forested region, the second largest in China (Hua et al., 2018), with forest cover
119 ranging from 3% to 92% (mean: 51%), influencing evapotranspiration and runoff
120 generation. Dominant soil types, according to the Genetic Soil Classification of China
121 (Shi et al., 2004), include purple soil (12.20%), yellow soil (11.39%), and red soil
122 (9.52%), each with distinct hydrological properties.



123

124 **Fig.1.** Geographical distribution of the 80 gauged catchments used, with locations of
 125 hydrometry station (red points) and major rivers indicated.

126 **2.2. Datasets**

127 Hourly flow data (2015–2018) for 80 mountainous catchments in China were
 128 sourced from the Hydrological Bureau of the Ministry of Water Resources, through
 129 China's hydrologic yearbooks, encompassing a spectrum of events from flash floods
 130 and general floods which can be derived from mountainous upland catchments. Hourly
 131 rainfall data (2015–2018) were obtained from ground meteorological stations across
 132 China (<http://en.weather.com.cn>), providing crucial input for hydrological modelling.
 133 Additional meteorological variables, including temperature, wind speed, dewpoint
 134 temperature, and surface net solar radiation, were obtained from the ERA5 hourly
 135 dataset (1940–present) (Hersbach et al., 2023), ensuring comprehensive atmospheric
 136 forcing. Relative humidity was estimated using dewpoint temperature. Historical

137 (1901–2021) and projected future (SSP585, 2022–2100) temperature and precipitation
138 data for China, averaged from the EC-Earth3, GFDL-ESM4, and MRI-ESM2-0 models
139 at 1 km resolution, were obtained from "A Big Earth Data Platform for Three Poles" to
140 assess the impact of climate change (Ding et al., 2020) (<http://poles.tpdc.ac.cn>).

141 Topographic data, including a 30-m resolution Digital Elevation Model (DEM), used
142 for river network and topographic index derivation, were obtained from EARTHDATA
143 and used for river network delineation and topographic index derivation
144 (<https://search.earthdata.nasa.gov/search>). Forest cover data (30-m resolution) were
145 sourced from the Global Forest Cover and Forest Change Map
146 (<https://www.noda.ac.cn/>), providing information on vegetation characteristics. Bulk
147 density (BD) data were derived from the Soil Database of China for Land Surface
148 Modelling (Dai et al., 2013). Soil hydraulic parameters, specifically saturated hydraulic
149 conductivity (Ks_CH) for Clapp and Hornberger functions and the pore-connectivity
150 parameter (L) for van Genuchten and Mualem functions, were acquired from the China
151 Dataset of Soil Hydraulic Parameters Using Pedotransfer Functions for Land Surface
152 Modeling (Shangguan et al., 2013).

153

154

155

156

157

158

159 **Table 1.** Model forcing data and catchment descriptors information.

Data type	Name	Unit	Function
	Rainfall	mm	Input for hydrological model
	Flood	m ³ /s	Used for model calibration (hourly resolution)
Hydro-meteorology	Temperature	K	Input for hydrological model
	Surface pressure	Pa	
	Dewpoint temperature	K	
	wind speed	m/s	
	Surface net solar radiation	J/m ²	
	Relative humidity	%	
	1 km monthly precipitation (1901-2021)	mm	Multi-year surface average as catchment descriptors
	1 km monthly temperature (1901-2021)	°C	
	1 km monthly temperature (2022-2100, SSP5-8.5, EC-Earth3, GFDL-ESM4, MRI-ESM2-0)	°C	
	1 km monthly precipitation (2022-2100, SSP5-8.5, EC-Earth3, GFDL-ESM4, MRI-ESM2-0)	mm	
	Soil bulk density (BD)	g/cm ³	
Soil characteristics	Pore-connectivity parameter (L) for the van Genuchten and Mualem functions	-	Surface average as catchment descriptors
	Saturated hydraulic conductivity (Ks_CH) of the Clapp and Hornberger Functions	cm d ⁻¹	
	Forest cover (FC)	%	
Topography	DEM	m	
	Topographic index	-	
	Slope	mm ⁻¹	
	Catchment area	km ²	

160

3. Methodology

161

3.1. Hydrological model

162 Top-SSF is a semi-distributed hydrological model based on the well-established
 163 TOPMODEL framework, which delineates sub-basins based on the topographic index.
 164 It retains the key advantages of TOPMODEL, such as its parsimonious structure,
 165 physical interpretability, and ease of parameter transfer (Beven et al., 2021; Gao et al.,
 166 2018), consists of 15 parameters representing six key hydrological components: canopy
 167 interception, infiltration, evapotranspiration, unsaturated zone moisture transport,
 168 subsurface storm flow, and flow routing (Li et al., 2024). In the Top-SSF model, flood
 169 can be comprised of four components: infiltration-excess overland flow, saturation-
 170 excess overland flow, subsurface storm flow, and groundwater discharge.

171 Infiltration-excess overland flow occurs when the rainfall intensity exceeds the
 172 infiltration capacity. In this study, infiltration is simulated using the Green-Ampt model.
 173 When surface ponding occurs, the infiltration rate is determined by solving the Green-
 174 Ampt equation iteratively, for which the Newton-Raphson method is employed. The
 175 infiltration rate (f_{in}) is given by:

$$176 \quad f_{in} = -\frac{Ks(CD+F_{satrt})}{Szm(1-e^{(F_{satrt}/Szm)})} \quad (1)$$

177 where, f_{in} is the infiltration rate (m/h); Ks is surface hydraulic conductivity (m/h);
 178 CD is capillary drive (m); F_{satrt} is the initial cumulative infiltration (m); Szm is the
 179 maximum water storage capacity in the unsaturated zone (m).

180 Saturation excess overland flow occurs at computational cell i when the
 181 groundwater table depth, S_i is less than or equal to zero (i.e., $S_i \leq 0$, indicating the
 182 water table has reached the surface). It is calculated as:

$$183 \quad r_{s,i} = \max\{Suz_i - \max(S_i, 0), 0\} \quad (2)$$

184 where, $r_{s,i}$ is the depth of saturation excess overland flow generated at cell i (m); Suz_i
 185 is the soil water storage in the unsaturated zone, at cell i (m); S_i is the groundwater table
 186 depth at cell i (m).

187 The depth of subsurface storm flow generated at computational cell i , $r_{sf,i}$ is
 188 given by:

$$189 \quad r_{sf,i} = q_{sf0}(1 - S_{sf,i}/S_{fmax}) \quad (3)$$

190 where, $r_{sf,i}$ is the depth of subsurface storm flow at cell i (m); q_{sf0} is initial subsurface
 191 storm flow (m); $S_{sf,i}$ is the water storage deficit in the subsurface storm flow zone at
 192 cell i (m).

193 The depth of groundwater discharge is calculated as:

$$194 \quad r_b = e^{\ln Te - \lambda - \bar{S}_g/Szm} \quad (4)$$

195 where, r_b is depth of groundwater discharge (m); $\ln Te$ is the log of the areal average of
 196 $T0$ (m^2/h); λ is the catchment average topographic index; \bar{S}_g is the catchment average
 197 groundwater table depth (m). For the complete set of equations for the Top-SSF model,

198 the reader is referred to the Supplementary Material and (Li et al., 2024).

199

200 **3.2. Multi-machine learning ensemble method**

201 To improve flood prediction accuracy in ungauged mountainous catchments, we

202 proposed a multi-machine learning ensemble method for regionalizing sensitive

203 parameters of the Top-SSF model. This method leverages the complementary strengths

204 of multi-machine learning methods to estimate model parameters based on catchment

205 descriptors (Fig. 2). The characteristics, strengths, and limitations of each machine

206 learning method are summarized in Table 2. The ensemble method employs a cross-

207 validation procedure to select the best-performing machine learning method for each

208 sensitive parameter. These selections are then integrated into a unified regionalization

209 scheme. By mitigating limitations inherent in single machine learning regionalization,

210 such as model bias and overfitting, and by capturing complex hydrological processes

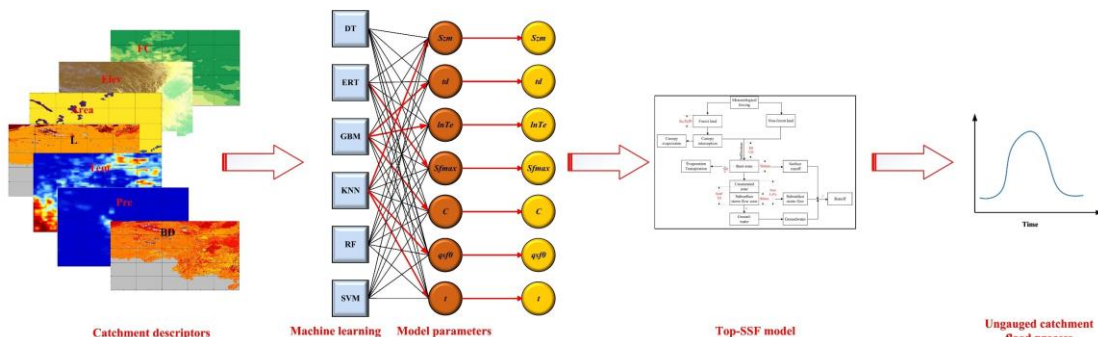
211 in mountainous catchment, this ensemble method aims to achieve more accurate flood

212 prediction in ungauged catchments.

213

Table 2. Seven machine learning model characteristics, advantages and disadvantages.

Machine learning	Characteristic	Advantage	Disadvantages
DT	A single decision tree hierarchically partitions the data space using a tree structure, with internal nodes representing features, branches representing decision rules, and leaf nodes representing class labels.	High interpretability; Minimal data preprocessing.	Unstable; Tends to overfit.
ERT	Construct multiple decision trees with randomly selected feature values and randomly divided nodes (Geurts et al., 2006).	Low overfitting risk; Computational efficiency; Resilient to noise.	Possibility of increased bias; Limited interpretability.
GBM	Construct multiple decision trees. Multiple weak learners are trained iteratively and the loss function is optimised using gradient descent, progressively combined into a robust model through the learning rate (Friedman, 2002).	High accuracy for structured data; Robust to outliers; Minimal data preprocessing.	Limited interpretability; Complex adjustments.
KNN	It is a non-parametric, instance-based supervised learning algorithm. It operates by finding the K nearest data points in the training data to a given data point and making predictions based on these (Wani et al., 2017).	Simple and easy to implement. Learning process is quick.	Sensitivity to noisy and scale of data. Accuracy can be heavily impacted by the choice of K.
RF	A bagging algorithm proposed by Breiman (2001) that uses ensemble learning. Involves training numerous decision trees and aggregating predictions.	Simple and easy to implement; Low computational cost.	Prone to overfitting in noisy regression tasks.
SVM	Identifies hyperplanes in high-dimensional spaces to segregate data. The optimal hyperplane maximizes the margin between it and the nearest data points, termed support vectors (Sain, 1996).	Uses kernel functions to address nonlinear classification issues.	Sensitive to noise

**Fig.2.** Multi-machine learning ensemble method for regionalization in ungauged mountainous catchments. The red line indicates the machine learning method that yielded the optimal parameter estimates.**3.3. Parameter regionalization process**

The parameter regionalization process comprised four key steps: (1) Top-SSF model calibration and parameter sensitivity analysis; (2) selection of relevant catchment descriptors; (3) establishment of regionalization relationships between sensitive model parameters and catchment descriptors using multi-machine learning ensemble methods;

224 and (4) evaluation of parameter regionalization performance.

225 **3.3.1. Top-SSF model calibration and parameter sensitivity analysis**

226 In this study, the Top-SSF model was employed to simulate hydrological processes.

227 The model was driven by continuous hourly meteorological data, including rainfall,

228 temperature, surface pressure, relative humidity, wind speed, and surface net solar

229 radiation. For each catchment, model parameters were calibrated using two

230 hydrologically independent and representative flood events. A third, distinct flood

231 event was then used for model validation. The Nash-Sutcliffe Efficiency (NSE) served

232 as the objective function during calibration, with parameter optimization achieved

233 using the Shuffled Complex Evolution (SCE-UA) algorithm (Duan et al., 1994), known

234 for its global convergence and robustness (Dakhlaoui et al., 2012; Qi et al., 2016).

235 Model performance was evaluated using the NSE, the relative error of flood peak flow

236 (Q_p), and the absolute error in flood peak occurrence time (T_p), following China's

237 Specification for Hydrological Information Forecast (GB/T 22482-2008). These

238 metrics quantify the model's ability to predict flood dynamics, peak flow, and timing.

239 Following calibration, a sensitivity analysis was conducted to identify and exclude

240 insensitive model parameters (Lenhart et al., 2002), which were then used for

241 regionalization. This approach reduces the dimensionality of the regionalization

242 problem and improves the efficiency of the process.

243 The sensitivity index (Si) of each hydrological model parameter was determined

244 using the method of Lenhart et al. (2002), which assesses the influence of $\pm 10\%$

245 changes in parameter values (Eq. 1). Table 3 outlines the sensitivity analysis results for

246 the model parameters across the 80 mountainous catchments. The Si values are
 247 categorized as follows (Guo et al., 2022): negligible sensitivity ($|Si| < 0.05$),
 248 moderate sensitivity ($0.05 < |Si| < 0.2$), high sensitivity ($0.2 < |Si| < 1.00$), and
 249 extremely high sensitivity ($|Si| \geq 1.00$). Based on the sensitivity analyses, seven
 250 sensitive model parameters were identified: Szm , $lnTe$, $Sfmax$, C , $qsf0$, t (Table 3).

$$251 \quad Si = \frac{1}{N} \sum_t^N \frac{(y_2(t) - y_1(t))/y_0(t)}{2\Delta x/x_0} \quad (5)$$

252 where $y_0(t)$ is the flood value of the calibrated parameter x_0 at time t ; Δx is the
 253 adjusted parameter difference, $\Delta x/x_0=10\%$; $y_1(t)$ is the flood value of the calibrated
 254 parameter $x_0 - \Delta x$ at time t ; $y_2(t)$ is the flood value of the calibrated parameter $x_0 +$
 255 Δx at time t .

256 **Table 3.** Top-SSF model main modules and default range of parameters.

Modular	Parameter	Definition	Unite	Default range	Sensitivity index
Canopy interception	Sc	Canopy storage capacity	m	0.00~0.01	<0.05
	St	Trunk storage capacity	m	0.00~0.01	<0.05
	Pt	Proportion of rain diverted into stemflow per cover	%	0.00~1.00	<0.05
Evapotranspiration	$Sr0$	Initial root zone storage deficit	m	0.00~0.02	<0.05
	$Srmax$	Maximum root zone storage deficit	m	0.00~2	<0.05
Infiltration	Ks	Surface hydraulic conductivity	m/h	0~0.01	<0.05
	CD	Capillary drive (Morel-Seytoux et al., 1974)	m	0~5	<0.05
Unsaturated zone	$Suz0$	Initial baseflow per unit area	m	0.00~ 10^{-4}	<0.05
	Szm	Soil maximum water storage capacity	m	0.00~1.00	0.19
	td	Unsaturated zone time delay per unit storage deficit	h/m	0~3	1.07
	$lnTe$	log of the areal average of $T0$	m^2/h	-2.00~1.00	3.4
Subsurface storm flow zone	$Sfmax$	Maximum subsurface storm flow zone deficit	m	0.00~0.01	0.16
	C	Transfer coefficient	m^{-2}/h	0.00~0.1	0.26
	$qsf0$	Initial subsurface storm flow per unit area	m	0.00~0.02	0.18
Routing	t	Flow routing correction coefficient	-	0.00~5.0	1.21

257 **Note, the bolded values in the sensitivity index indicate sensitive model parameters.**

258 **3.3.2. Catchment descriptor selection**

259 To mitigate the effects of multicollinearity on the accuracy and reliability of the
260 parameter regionalization methods, catchment descriptors were screened using the
261 variance inflation factor (VIF) and correlation coefficients. A VIF threshold of less than
262 10 (VIF < 10) was used to indicate acceptably low multicollinearity (Salmeron et al.,
263 2018). Initial screening identified strong correlations between several descriptor pairs,
264 notably L with Ks_CH, and Tem with Elev. Furthermore, the VIF values for Ks_CH
265 and Slope were found to exceed 10. Consequently, Ks_CH and Slope were removed
266 from the potential set of descriptors. Following their removal, a re-evaluation of the
267 VIF for the remaining descriptors was conducted. Although a notable correlation exists
268 between Tem and elevation (Elev), their VIF values in the reduced set were both below
269 the threshold of 10. Given the importance of Tem for representing climate impacts and
270 Elev as a key topographic driver, both were retained to preserve potentially valuable
271 information. The final set of seven catchment descriptors selected for regionalization
272 therefore comprised FC, Elev, Area, L, Tem, Pre, and BD. As illustrated in Fig. 3b, the
273 correlations among these final descriptors and the sensitive model parameters are
274 generally low (highest at 0.5), suggesting that the relationships are complex and
275 nonlinear.



276
277 **Fig.3.** Analysis of catchment descriptor relationships: (a) Correlation coefficients and variance
278 inflation factors (VIF) among all descriptors; (b) Correlation coefficients between
279 sensitivity model parameters and descriptors with VIF values below 10.

280 **3.3.3. Parameter regionalization**

281 To simulate ungauged catchment conditions, each of the 80 catchments was
282 iteratively treated as an ungauged catchment, with the remaining 79 catchments serving
283 as donor catchments. A parameter regionalization method was then constructed using
284 the catchment descriptors and sensitive model parameters of the donor catchments to
285 predict the seven sensitive model parameters for the ungauged catchment based on its
286 catchment descriptors. These predicted model parameters were then input into the Top-
287 SSF model to enable flood prediction in ungauged catchments. To ensure robust and
288 generalizable results, K-fold cross-validation ($K = 10$) was implemented. This involved
289 randomly partitioning the 79 donor catchments into K subsets, using one subset as a
290 test set and the remaining $K-1$ subsets for method training in each iteration (Jung, 2018).
291 This approach maximizes data utilization and minimizes bias associated with specific
292 data partitioning. Hyperparameter tuning for each machine learning method was
293 performed using RandomizedSearchCV (Bergstra et al., 2012), with the objective of
294 minimizing the difference between predicted and observed parameter values.

295 **3.3.4. Evaluated metrics**

296 The performance of the parameter regionalization methods was evaluated by
 297 considering two key aspects. First, the accuracy of the methods in estimating sensitive
 298 model parameters was assessed using three metrics: root mean square error (RMSE),
 299 standard deviation (STD), and the coefficient of determination (R^2). The R^2 was used
 300 to quantify the agreement between estimated and calibrated parameter sets. Second, to
 301 evaluate the impact of parameter regionalization on flood prediction. The resulting
 302 flood predictions were then evaluated using the NSE, Qp, and Tp metrics.

$$303 NSE = 1 - \frac{\sum_{j=1}^M (Q_{obs}(j) - Q_{sim}(j))^2}{\sum_{j=1}^M (Q_{obs}(j) - \bar{Q}_{obs})^2} \quad (6)$$

$$304 Q_p = \left| \frac{Q_{obs,p} - Q_{sim,p}}{Q_{obs,p}} \times 100\% \right| \quad (7)$$

$$305 T_p = |T_{obs,p} - T_{sim,p}| \quad (8)$$

306 where $Q_{obs}(j)$ is the observed flow rate (m^3/s); $Q_{sim}(j)$ is the simulated flow rate
 307 (m^3/s); \bar{Q}_{obs} is the mean value of the observed flow rate (m^3/s); $Q_{obs,p}$ is the observed
 308 flood peak flow (m^3/s); $Q_{sim,p}$ is the simulated flood peak flow (m^3/s); $T_{obs,p}$ is the
 309 observed flood peak occurrence time (h); and $T_{sim,p}$ is the simulated flood peak
 310 occurrence time (h).

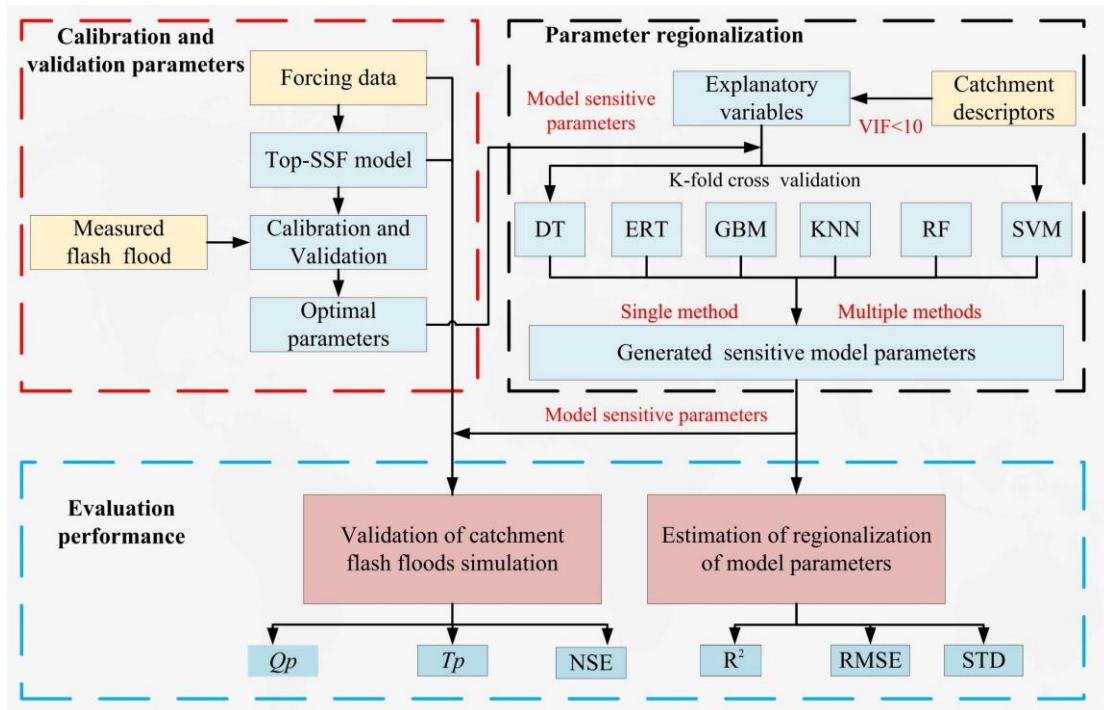
311

$$312 RMSE = \sqrt{\frac{1}{N} \sum_{i=1}^n (X_i - Y_i)^2} \quad (9)$$

$$313 STD = \sqrt{\frac{1}{N-1} \sum_{i=1}^N (Y_i - \bar{Y})^2} \quad (10)$$

$$314 R^2 = \frac{[\sum_{i=1}^n (X_i - \bar{X})(Y_i - \bar{Y})]^2}{\sum_{i=1}^n (X_i - \bar{X})^2 \sum_{i=1}^n (Y_i - \bar{Y})^2} \quad (11)$$

315 where X_i is the Top-SSF calibration model parameter value; Y_i is the model parameter
 316 estimated value using the parameter regionalization method; \bar{X} and \bar{Y} are the mean
 317 values of X_i and Y_i ; N is the sample size equal to 80.



318

319 **Fig.4.** Flowchart illustrating the parameter calibration, validation, and regionalization workflow.
 320 Abbreviations: Top-SSF (Topography-Based Subsurface Storm Flow hydrological model),
 321 DT (Decision Tree), ERT (Extremely Randomized Trees), GBM (Gradient Boosting
 322 Machine), KNN (K-Nearest Neighbor), RF (Random Forest), SVM (Support Vector
 323 Machine), NSE (Nash-Sutcliffe efficiency), R^2 (Coefficient of Determination), Q_p (The
 324 relative error of flood peak flow), T_p (The absolute error in flood peak occurrence time),
 325 VIF (Variance inflation factor), RMSE (Root mean square error), STD (Standard
 326 deviation).

327

4. Result

328

4.1. Model performance

329

The Top-SSF model demonstrated good flood simulation performance across the

330

80 gauged catchments, as quantified by NSE, Q_p , and T_p . During the calibration period,

331

50% of the catchments achieved NSE values exceeding 0.78 (Fig. 5a), the median Q_p

332

value was below 10% (Fig. 5b), and the median T_p value was within 2 hours (Fig. 5c).

333

The average NSE value was approximately 0.8, with a maximum of 0.96. The majority

334

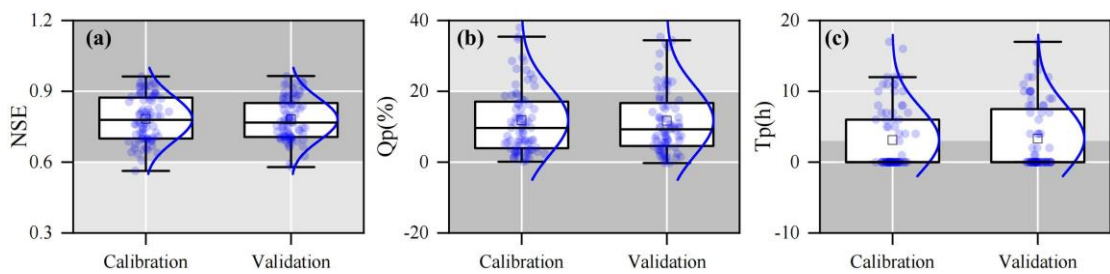
of Q_p values were around 8%, and the majority of T_p values were below 2 hours.

335

During the validation period, the median NSE value was 0.76 (Fig. 5a), the median Q_p

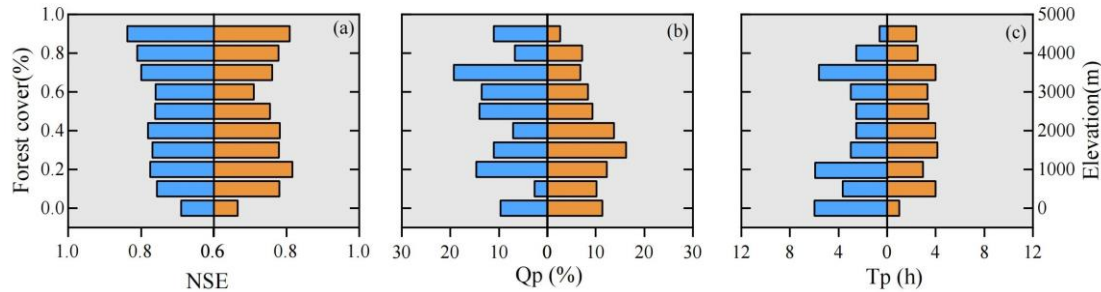
336 value was below 10% (Fig. 5b), and the median T_p value was within 4 hours (Fig.5c).
 337 The hydrological response times for the 80 catchments were approximated as the time
 338 from precipitation peak to flood peak. The estimated range is from 1 to 26 hours. This
 339 diversity is indicative of the comprehensive nature of the study, which encompasses
 340 both rapid flash floods in smaller basins and more general floods in larger, mountainous
 341 catchments (mean area: 1,586 km²). For catchments with longer response times, a
 342 median error of 2-4 hours remains operationally valuable for providing sufficient flood
 343 warning lead time. It is noteworthy that the median T_p during the calibration period
 344 (within 2 hours) satisfied China's Specification for Hydrological Information Forecast
 345 (GB/T 22482-2008) stringent requirements for high-quality forecasts.

346 Model performance also exhibited some dependence on catchment characteristics.
 347 For instance, NSE generally improved with increasing forest cover (Fig. 6a), potentially
 348 due to the model's explicit representation of forest canopy interception and subsurface
 349 storm flow generation mechanisms. The relationship between NSE, Q_p , T_p and
 350 elevation was more complex, suggesting a nonlinear influence of elevation on model
 351 performance (Fig. 6 a-c). The demonstrated robust performance of the Top-SSF model
 352 provides a strong foundation for its application in subsequent parameter regionalization
 353 analyses.



354
 355 **Fig. 5.** Boxplots of (a) NSE, (b) Q_p , and (c) T_p during the calibration and validation periods

356 for 80 gauged catchments. The box represents the interquartile range, with the middle line
 357 indicating the median (50th percentile). The whiskers represent the minimum and
 358 maximum values. "□" represents the mean value. Dark grey indicates the range of flood
 359 prediction criteria (i.e., $NSE > 0.75$, $Qp < 20\%$, and $Tp < 2$ hours).



360
 361 **Fig.6.** Influence of environmental factors on Top-SSF model performance in flood simulation. The
 362 graphs illustrate the relationship between model evaluation metrics and forest cover (left) and
 363 elevation (right)."
 364

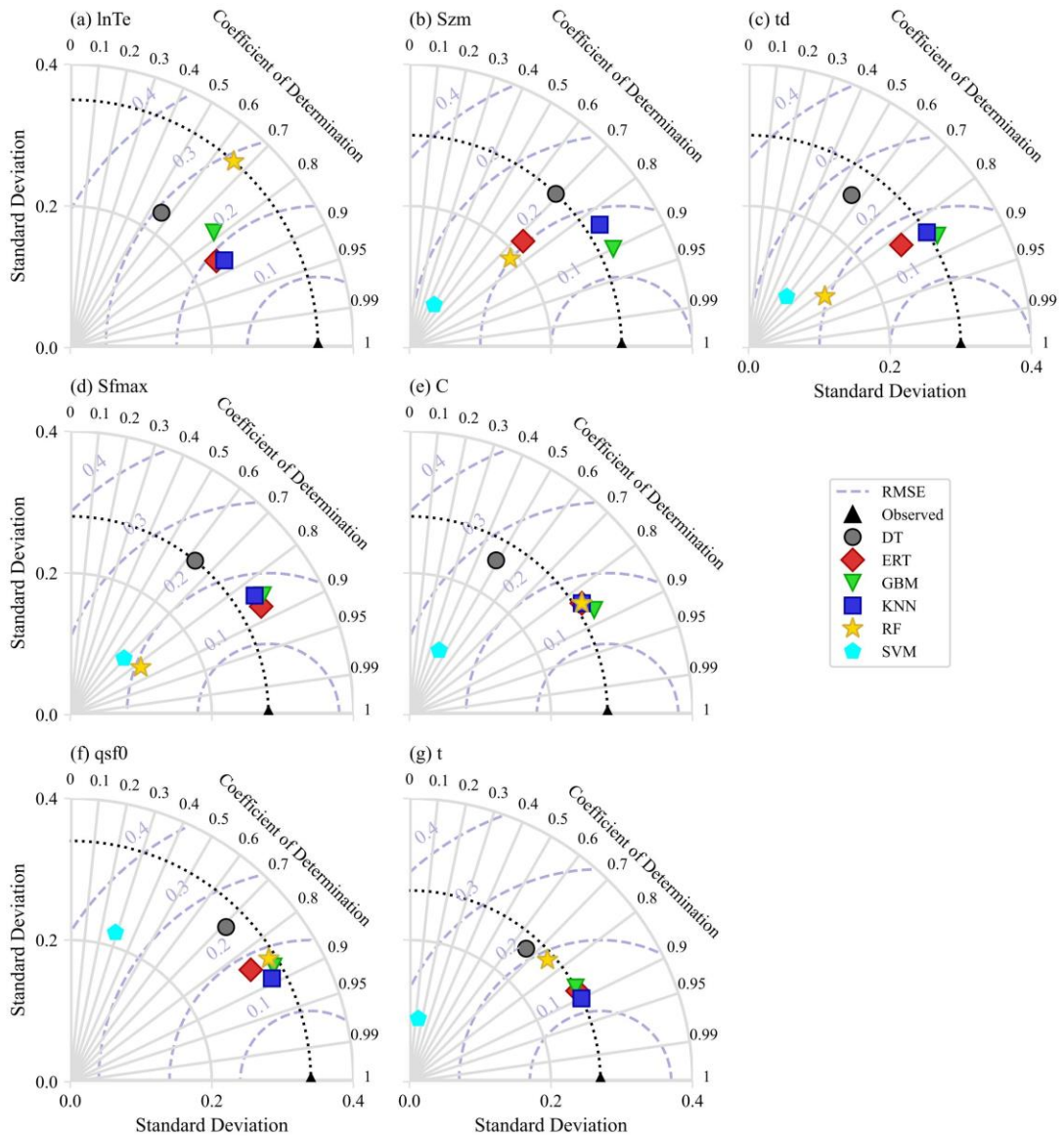
365 **4.2. Results of parameter regionalization**

366 **4.2.1. Comparison of sensitive model parameter estimates**

367 The six single machine learning regionalization methods exhibited varying
 368 performance in estimating sensitive model parameters (Fig. 7), likely due to differences
 369 in catchment descriptor characteristics and the underlying principles of each method.

370 Their hyperparameter results are presented in Tables S1–S6 of the supplementary
 371 material. The GBM demonstrated the highest accuracy in estimating Szm , td , and C
 372 ($R^2 = 0.90$, 0.86, and 0.87, respectively,), with its estimates also exhibiting a STD that
 373 closely matched the distribution of the calibrated parameter values. KNN provided the
 374 most accurate estimates for $lnTe$, $qsf0$, and t ($R^2 = 0.87$, 0.89, and 0.90, respectively),
 375 also with STD closely resembling the calibrated parameter distributions. ERT
 376 performed best in estimating $Sfmax$ ($R^2 = 0.87$), but its performance was generally
 377 poorer for other parameters. DT, SVM, and RF methods generally showed lower
 378 performance across all sensitive model parameters. These differences in performance
 379 highlight the potential benefits of multi-machine learning ensemble methods for

380 improving flood prediction in ungauged mountainous catchments.



382 **Fig.7.** Performance of parameter regionalization methods assessed using Taylor diagrams. The
383 diagrams show the accuracy of sensitive model parameter estimates, with the coefficient
384 of determination (R^2) indicated by the radial axis, standard deviation (STD) by the
385 horizontal and vertical axes, root mean square error (RMSE) by the grey-blue dotted lines,
386 and the standard deviation of observations by the black dotted line."

387 4.2.2. Comparison of flood forecasting results

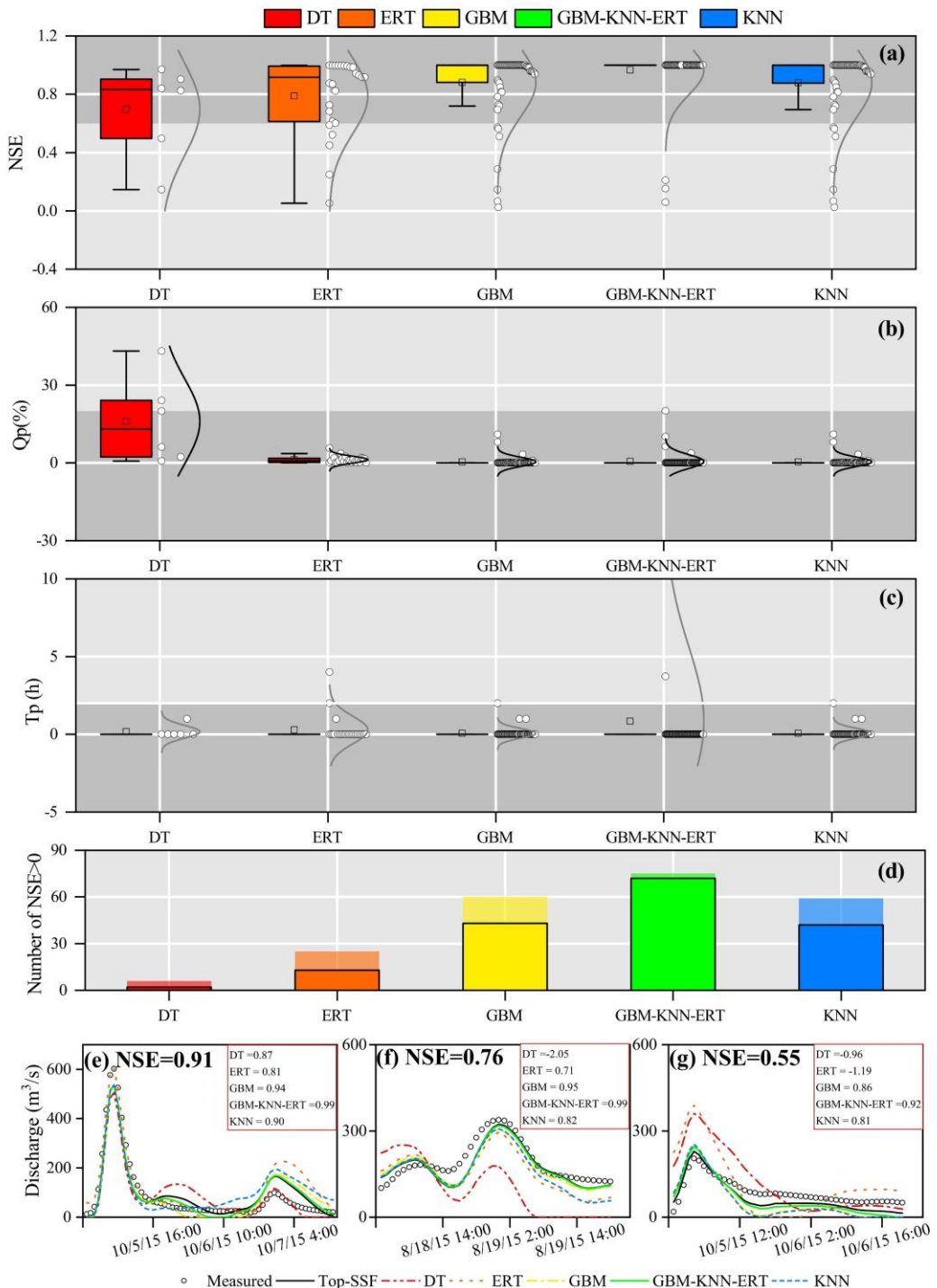
388 The flood prediction performance of the Top-SSF model, integrated with different
389 parameter regionalization methods, was compared across 80 mountainous catchments
390 in southwestern China. The methods included single machine learning methods and a

391 multi-machine learning ensemble method (GBM-KNN-ERT), where GBM estimated
392 Szm , td , and C ; KNN estimated $lnTe$, $qsf0$, and t ; and ERT estimated $Sfmax$. The
393 performance of these parameter regionalization methods was then evaluated against the
394 performance of the Top-SSF model using calibrated parameters. Among the single
395 machine learning methods, GBM performed best, with 60 catchments achieving a
396 positive NSE (NSE > 0, Fig. 8d). Critically, for high-accuracy predictions (NSE > 0.9),
397 GBM succeeded in 43 catchments (54%), also showing strong performance with Qp
398 less than 5% and Tp less than 1 hour in most cases (Fig. 8a-c). The GBM-KNN-ERT
399 ensemble method yielded even better results. It increased the number of catchments
400 with positive NSE to 75 (Fig. 8d). More impressively, the ensemble method achieved
401 exceptional performance (NSE > 0.9) in 72 catchments (90%). This represents a 67.44%
402 increase in the number of high-accuracy predictions compared to the best single method
403 (GBM). Furthermore, the ensemble method Qp values were more concentrated around
404 zero, and 90% of catchments maintained near-zero Tp values. These results strongly
405 demonstrate the superior potential of multi-machine learning ensembles for improving
406 flood prediction in ungauged catchments.

407 To further illustrate these performance differences visually, Fig. 8 (e, f, and g)
408 presents hydrographs from three randomly selected flood events. These events
409 represent cases where the calibrated Top-SSF model itself achieved high (NSE=0.91),
410 medium (NSE=0.76), and low (NSE=0.55) performance, respectively. A key insight
411 from these plots is that the Top-SSF simulation (solid black line) is the performance
412 benchmark for the regionalization methods. Although the models aim to approximate

413 measured floods, their performance is ultimately limited by the accuracy of the Top-
414 SSF model structure and its optimized parameters.

415 The hydrographs show how the GBM-KNN-ERT ensemble achieves superior
416 performance by leveraging the complementary strengths of its component methods. For
417 instance, in the high-performance case (Fig. 8e), the GBM and KNN methods capture
418 the overall shape well, but the ERT simulation provides a more precise estimation of
419 the primary flood peak. The final ensemble successfully integrates this peak accuracy,
420 resulting in the highest overall performance. Similarly, Fig. 8f shows that the ensemble
421 moderates the slow initial rise characteristic of the KNN method, leading to a more
422 realistic rising limb. The ensemble method ability to balance competing errors is most
423 evident in the low-performance case (Fig. 8g). During the recession phase, the ensemble
424 method averages the high bias of the ERT method with the low bias of the GBM and
425 KNN methods, producing a hydrograph that more closely resembles the benchmark
426 simulation than any single model could. This synergy demonstrates that the ensemble
427 method superior performance is a direct result of its ability to integrate the specific,
428 complementary strengths of each member model across different parts of the
429 hydrological process.



430

431

432

433

434

435

436

437

438

439

Fig.8. Evaluation of flood prediction performance for different parameter regionalization methods. (a-c) show the distributions of Nash-Sutcliffe Efficiency (NSE), relative peak flow error (Qp), and peak time error (Tp) across all 80 catchments, with shaded regions indicating where flood prediction standards were met ($\text{NSE} > 0.75$, $\text{Qp} < 20\%$, and $\text{Tp} < 2$ hours). (d) shows the number of catchments with $\text{NSE} > 0$ and the black border indicates the number of catchments with $\text{NSE} > 0.9$. (e-g) present example hydrographs comparing the simulated flood from each regionalization method against measured flood flow and the calibrated Top-SSF model benchmark for catchments where the benchmark model performance was (e) high ($\text{NSE}=0.91$), (f) medium ($\text{NSE}=0.76$), and (g) low ($\text{NSE}=0.55$).

440 **5. Discussion**

441 **5.1. Reliability of multi-machine learning ensemble in parameter regionalization**

442 In this study, the GBM-KNN-ERT method demonstrated superior regionalization
443 performance, highlighting the potential of ensemble methods for improving
444 hydrological predictions in ungauged mountainous catchments. The success of the
445 ensemble is rooted in the distinct learning mechanisms and behaviors of its individual
446 components, which were revealed during hyperparameter optimization.

447 The GBM method exhibited distinct parameter-specific sensitivities to
448 hyperparameters (Fig. 9a-c). For parameter C , the negative correlation between R^2 and
449 $n_estimators$ (>300 trees) indicates overfitting risks when modeling complex rainfall-
450 runoff interactions in heterogeneous mountainous terrain (Fig. 9a). This aligns with
451 previous findings emphasizing the need for complexity control in hydrological
452 generalization (Schoups et al., 2008). Conversely, the improved R^2 for parameter td
453 with increased $n_estimators$ highlights the capacity of ensemble learning to capture
454 complex, nonlinear relationships between catchment descriptors and hydrological
455 parameters (Hastie et al., 2009). The contrasting optimal max_depth of 5 layers for
456 parameter C , compared to shallower optimal depths (3 layers) for Szm and td , suggests
457 that parameters governing more complex hydrological processes in mountainous
458 catchments may require deeper decision trees to effectively capture the interactions
459 between climate, topography, and soil properties (Wainwright et al., 2013).

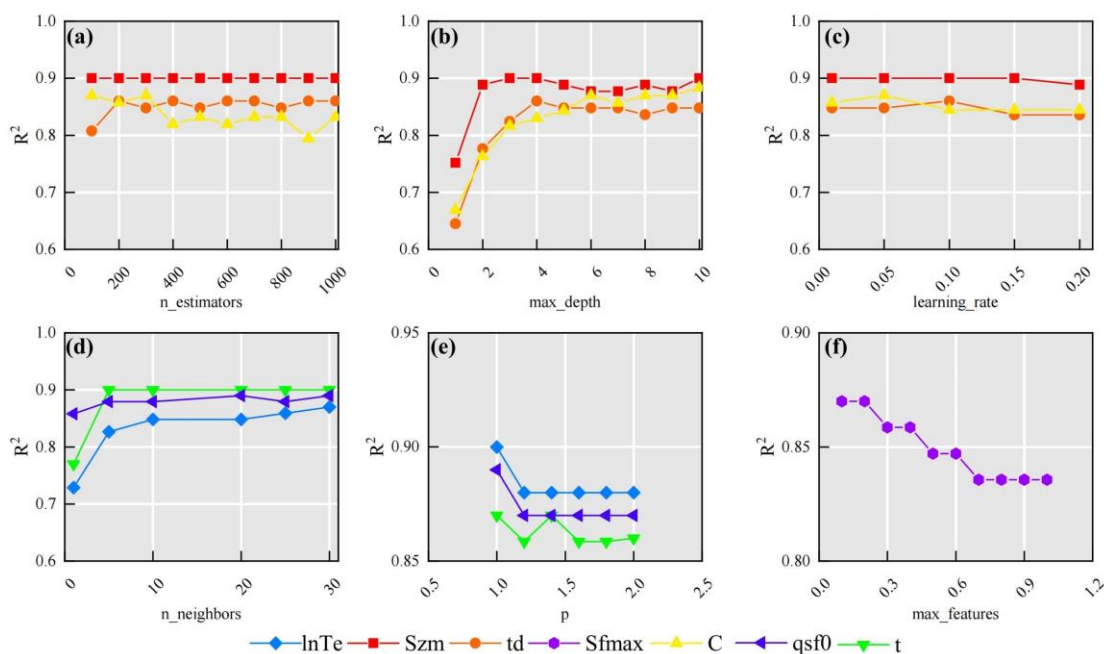
460 KNN performance exhibited pronounced sensitivity to neighbourhood size
461 ($n_neighbors$) and distance metric (p), highlighting the spatial heterogeneity of

462 catchment descriptors. For parameters $lnTe$ and $qsf0$, optimal performance was
463 observed at $n_neighbors = 30$ (Fig. 9d), aligns with the hypothesis that meaningful
464 hydrological similarities can emerge even in topographically complex mountainous
465 regions when considered at broader spatial scales (Li et al., 2022). Conversely,
466 parameter t achieved peak accuracy at $n_neighbors=5$, suggesting that localized, short-
467 term weather events and fine-scale topographic similarities in adjacent mountainous
468 areas can significantly influence local runoff processes (Garambois et al., 2015). The
469 Manhattan distance metric ($p=1$) outperformed Euclidean distance across all
470 parameters (Fig. 9e). This superiority stems from its ability to mitigate the "curse of
471 dimensionality" (Bellman, 1961) in high-dimensional datasets, a common
472 characteristic of mountainous catchments. In such datasets, sparse data distributions
473 and the presence of mixed variable types (e.g., topographic indices, land cover) can
474 significantly degrade the discriminative power of Euclidean distance (Rockström et al.,
475 2023). The robustness of the Manhattan distance arises from its axis-aligned sensitivity,
476 which provides a more effective means of handling feature scaling and integrating
477 catchment descriptors compared to the radial symmetry of Euclidean distance.

478 ERT performance was maximized at $max_features = 0.15$ (Fig. 9f). By restricting
479 the random sampling of features during node splits (using only 15% of the features),
480 both the diversity of the trees was enhanced and the effects of multicollinearity between
481 topographic and soil attributes were reduced. This finding aligns with the theory
482 proposed by Geurts et al. (2006), which suggests that random feature selection can
483 significantly improve model generalization, a particularly important consideration in

484 ungauged mountainous catchments characterized by high levels of inter-correlation
 485 among predictor variables.

486 These distinct sensitivities and learning mechanisms form the scientific basis for
 487 the superiority of the GBM-KNN-ERT method. As shown in Section 4.2, no single
 488 machine learning method is universally optimal for all hydrological model parameters.
 489 Instead, the ensemble method effectively allocates each parameter to the model best
 490 suited for its regionalization. Specifically, GBM, with its capacity for modeling
 491 complex interactions, proved optimal for integrated parameters like *Szm* and *td*. In
 492 contrast, the instance-based KNN was superior for parameters like *lnTe*, which are
 493 governed by physical similarity and spatial coherence. Finally, the highly randomized
 494 nature of ERT provided the necessary robustness to model the noisy relationship
 495 associated with the *Sfmax*. This synergistic combination, where each model
 496 contributes its unique strength, results in a final regionalization framework that is more
 497 accurate and physically plausible than any individual method operating in isolation.



498

499 **Fig.9.** Sensitivity of parameter estimation performance to key hyperparameters in (a-c) GBM,
500 (d-e) KNN method, and (f) ERT. (a) n_estimators (number of decision trees in GBM), (b)
501 max_depth (maximum depth of decision trees in GBM), (c) learning rate (GBM), (d)
502 n_neighbors (number of neighbors in KNN), (e) p-value of Minkowski distance (KNN;
503 p=1: Manhattan distance, p=2: Euclidean distance), and (f) max_features (ERT).

504

505 **5.2. Combining multiple machine learning methods for parameter regionalization**

506 Machine learning methods exhibit distinct strengths in hydrological parameter
507 estimation due to fundamental differences in data processing mechanisms, pattern
508 recognition strategies, and prediction generation (Bishop et al., 2006). This suggests
509 that multi-machine learning ensemble methods have the potential to synergistically
510 integrate advantages while effectively compensating for individual limitations, leading
511 to more robust and accurate parameter estimates. As demonstrated in Fig. 10, the GBM-
512 KNN-ERT method achieved notable improvements over any single machine learning
513 method, particularly for sensitive parameters $lnTe$, $Sfmax$, $qsf0$ and t , with R^2
514 increases ranging from 0.02 to 0.03 compared to the best-performing GBM method
515 (Fig.10e).

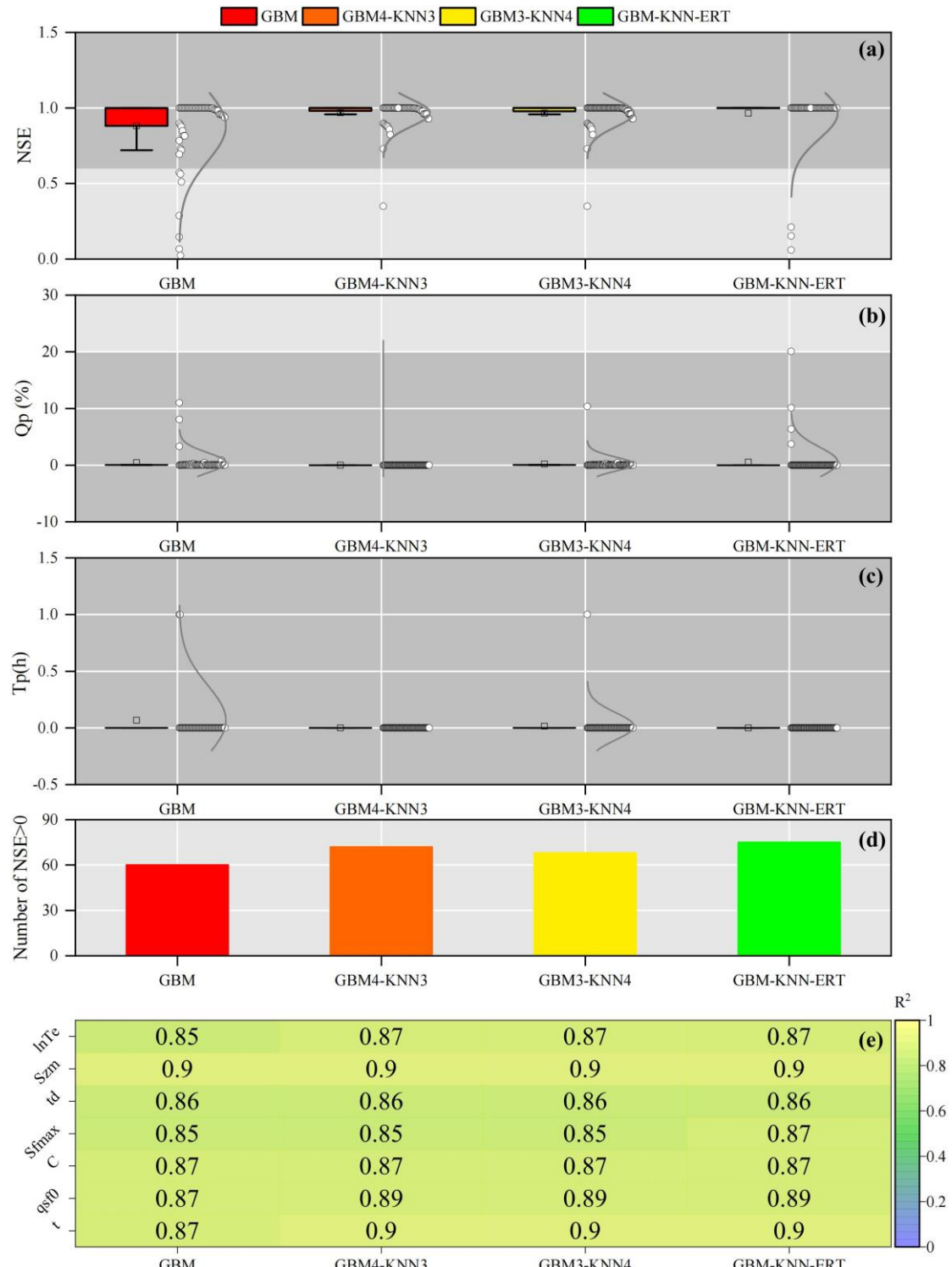
516 Interestingly, a comparison of GBM4-KNN3 (where $Sfmax$ is estimated by GBM)
517 and GBM3-KNN4 (where $Sfmax$ is estimated by KNN) revealed critical insights into
518 model parameter compatibility. Despite both achieving an identical R^2 of 0.85 for the
519 estimation of $Sfmax$, GBM4-KNN3 exhibited superior flood prediction performance,
520 with 72 catchments achieving $NSE > 0$ compared to only 68 catchments for GBM3-
521 KNN4. This suggests that GBM possesses an enhanced capability to resolve the
522 complex coupling between soil moisture dynamics and topography, leading to more
523 physically plausible representation of subsurface storm flow processes (Gupta et al.,

524 2023). The wider distribution of flood prediction performance observed for GBM3-
525 KNN4 (Fig. 10 a–c) further suggests that uncertainties introduced by KNN in the
526 estimation of $Sfmax$ may propagate nonlinearly during flood simulations, potentially
527 amplifying errors. This observation aligns with theoretical expectations that distance-
528 based methods may tend to oversmooth critical thresholds or sharp transitions in
529 heterogeneous environments, leading to a less accurate representation of hydrological
530 responses (Bellman, 1961).

531 Furthermore, an important consideration in adopting ensemble methods is the
532 trade-off between predictive accuracy and computational efficiency. To evaluate this
533 trade-off, we compared the model training times for various parameter regionalization
534 methods, with the results summarized in Table 4. The analysis shows that our proposed
535 GBM-KNN-ERT ensemble, while providing the highest predictive accuracy, required
536 a total training time of 102.8 s. This is moderately higher than the best-performing
537 single model, GBM (57.6 s), and other simpler ensemble methods like GBM4-KNN3
538 (36.1 s). The increased computational time for the GBM-KNN-ERT method is
539 primarily attributed to the inclusion of the ERT method for estimating the $Sfmax$,
540 which is inherently more computationally intensive than GBM or KNN.

541 However, it is crucial to contextualize this computational cost for operational use.
542 The process of training a regionalization method is an offline task, performed once to
543 establish the stable relationships between catchment descriptors and model parameters.
544 This one-time investment is not a constraint on real-time flood forecasting, as once the
545 method is trained, parameter estimation for a new ungauged catchment is nearly

546 instantaneous. Given this context, the modest increase in one-time training cost is a
547 justifiable investment for the significant improvements achieved in flood prediction
548 accuracy, model robustness, and stability. Therefore, for applications in water resource
549 management and flood risk assessment where high accuracy is paramount, the GBM-
550 KNN-ERT method strikes an optimal and practical balance between computational
551 efficiency and predictive performance.



552

553 **Fig.10.** Assessment of combined machine learning methods for improved parameter
 554 regionalization in ungauged mountainous catchments. Performance is evaluated against
 555 the GBM method, showing (a) NSE, (b) Qp, (c) Tp, (d) Number of catchments with $NSE >$
 556 0, and (e) the difference in R^2 .

557

558

559

560

561 **Table 4.** Running time (s) for different parameter regionalization methods

	GBM	GBM4-KNN3	GBM3-KNN4	GBM-KNN-ERT	KNN	ERT
<i>lnTe</i>	11.3	3.4	3.4	3.7	3.6	74.4
<i>Szm</i>	7.8	7.5	7.7	7.8	0.6	76.7
<i>td</i>	8.2	8.1	8.0	8.5	0.6	74.7
<i>Sfmax</i>	7.7	8.2	0.6	73.6	0.5	74.9
<i>C</i>	7.8	7.7	7.7	8.0	0.6	74.9
<i>qsf0</i>	7.4	0.6	0.6	0.6	0.6	76.3
<i>t</i>	7.4	0.6	0.6	0.6	0.5	75.3
Sum	57.6	36.1	28.6	102.8	7.0	527.2

562

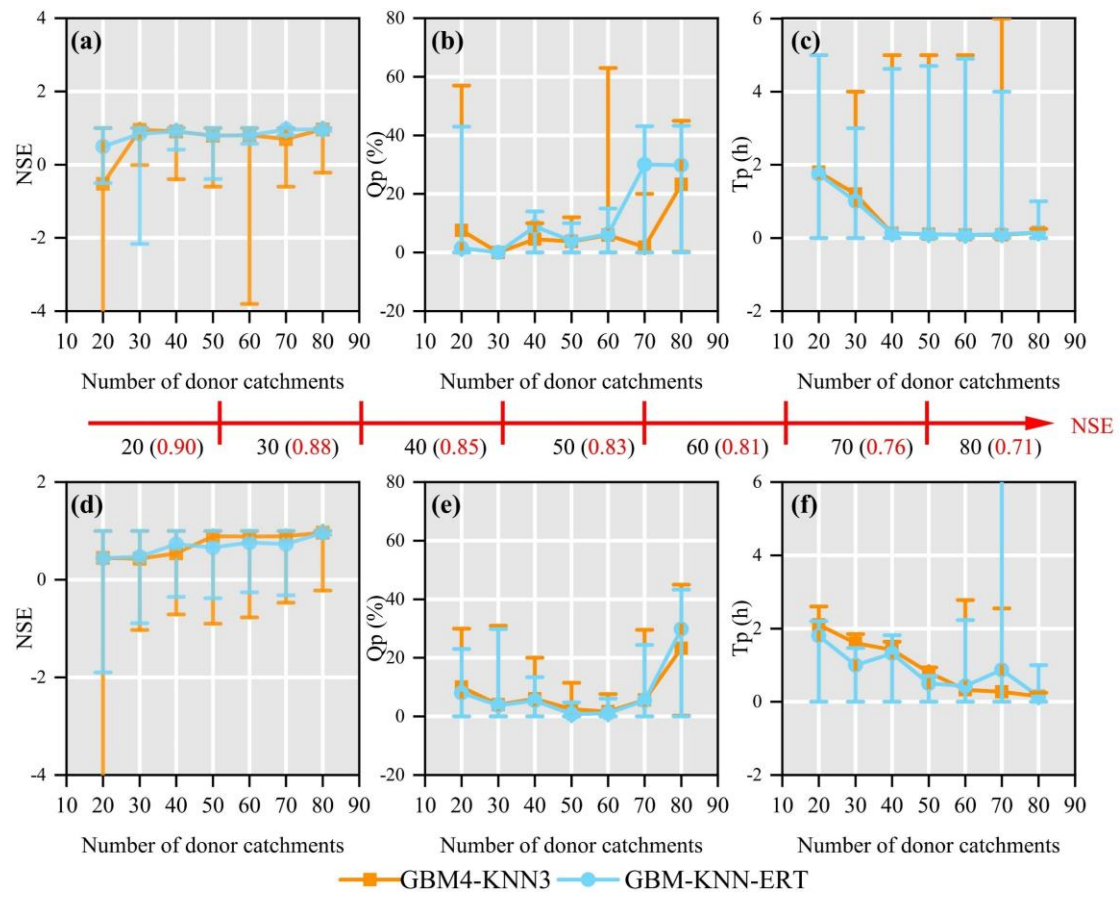
563 **5.3. The influence of donor catchment quantity on machine-learning parameter**
564 **regionalization**

565 The number of donor catchments used in machine learning-based parameter
566 regionalization methods is a critical factor influencing the accuracy and robustness of
567 hydrological predictions in ungauged catchments (Gauch et al., 2021; Song et al., 2022;
568 Zhang et al., 2022). In this study, we investigated the influence of donor catchment
569 quantity (ranging from 20 to 80) on the flood prediction performance of the two best-
570 performing parameter regionalization methods (GBM4-KNN3 and GBM-KNN-ERT)
571 across the 80 mountainous catchments (Fig 11). It is important to clarify that the
572 following analysis is not a method for selecting donor catchments based on physical
573 similarity—a task handled by the machine learning methods itself when it learns the
574 relationships between catchment descriptors and model parameters. Instead, this
575 experiment serves as a sensitivity analysis to understand how the regionalization
576 performance is affected by the overall quantity and quality of the available training data.

577 To systematically investigate the performance influence of donor catchment
578 quantity on parameter regionalization, two distinct sampling strategies were employed
579 across the 80 mountainous catchments. In Mode 1 (selection of donor catchments based
580 on decreasing NSE), which was designed to test the impact of data quality, a non-

581 monotonic relationship was observed. For both methods, regionalization performance
582 peaked with 20-40 donor catchments and then declined, particularly for the GBM4-
583 KNN3 method (Fig. 11a-c). This performance degradation is not due to increasing
584 catchment dissimilarity, but rather to the introduction of lower-quality training data. As
585 the donor pool expands beyond the best-performing catchments, it begins to include
586 catchments where the Top-SSF model calibration itself was less successful (i.e., lower
587 NSE values). These 'low-quality' samples may introduce noise and less reliable
588 parameter-descriptor relationships, which can mislead the training process (Gauch et
589 al., 2021; Zhang et al., 2022). Notably, the GBM-KNN-ERT method demonstrated
590 greater resilience to this degradation. Its performance, while also peaking early, did not
591 degrade as sharply and instead tended to stabilize after the inclusion of approximately
592 70 catchments. This suggests that the more complex ensemble structure has a superior
593 ability to suppress noise and generalize from a dataset containing a mix of high- and
594 low-quality examples, highlighting its enhanced robustness. In contrast, Mode 2
595 (random selection of donor catchments) demonstrated a consistent improvement in
596 regionalization performance for both NSE and Tp as the number of donor catchments
597 increased (Fig. 11d-f). However, while the average performance improves with data
598 quantity, it is important to acknowledge that this trend relies on the random samples
599 being generally representative; a poorly chosen random set could still reduce
600 generalizability. Notably, under both modes, the GBM-KNN-ERT method consistently
601 exhibited significantly greater performance stability compared to the alternative
602 ensemble, GBM4-KNN3. This enhanced robustness likely arises from its more

603 effective suppression of data heterogeneity and noise interference, indicating that more
 604 complex ensemble methods possess a greater capacity to balance the benefits of
 605 increased data quantity with the potential drawbacks of reduced data quality.



606
 607 **Fig. 11.** Performance comparison of two donor catchment selection methods for parameter
 608 regionalization as a function of donor catchment quantity. Mode1 (a-c) selects donor
 609 catchments in order of decreasing NSE, while Mode 2 (d-f) selects them randomly. Flood
 610 prediction accuracy is assessed using NSE, Qp, and Tp. Error bars represent the full range
 611 (minimum to maximum) of the performance metrics.

612 **5.4. The impact of climate change on parameter regionalization methods**

613 The hydrological cycle within catchments is fundamentally governed by complex
 614 interactions between climate and environmental factors. The Intergovernmental Panel
 615 on Climate Change (IPCC) has consistently documented a continuous and accelerating
 616 transition in global climatic patterns, characterized by increased variability and extreme
 617 events (Pachauri et al., 2014). Consequently, future flood predictions derived from

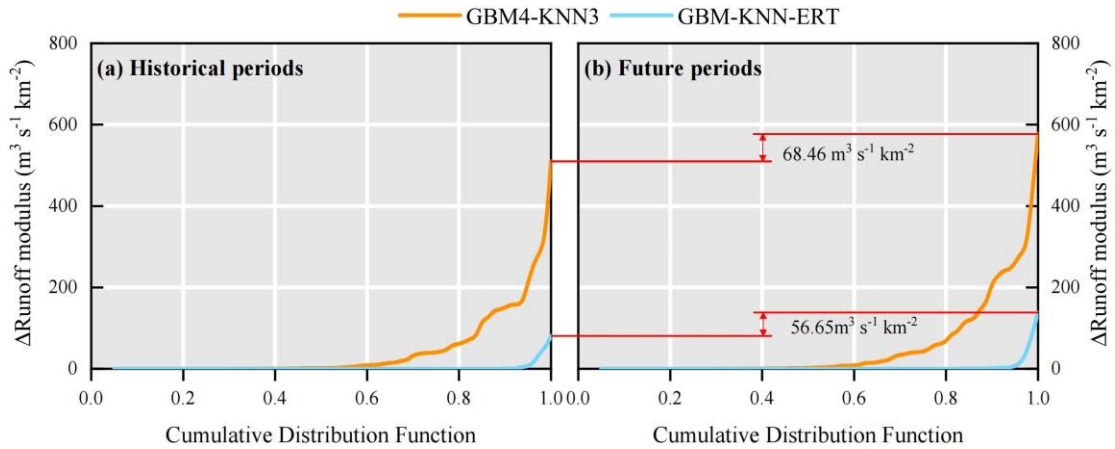
618 parameter regionalization methods are expected to exhibit increased uncertainty and
619 variability, highlighting the substantial influence of climate change on the reliability
620 and precision of flood predictions in ungauged mountainous catchments (Yang et al.,
621 2019). Therefore, a sensitivity analysis was designed to evaluate the robustness of the
622 trained regionalization models when confronted with climatic conditions outside their
623 original training range.

624 To quantitatively assess the impact of climate change, an experiment was devised
625 where this impact was primarily reflected through changes in two key catchment
626 descriptors: Tem and Pre. For the historical period, these descriptors represent the multi-
627 year averages over 1901–2021, while for the future period, they represent the projected
628 multi-year averages over 2022–2100 under the SSP5-8.5 scenario. The regionalization
629 methods (GBM4-KNN3 and GBM-KNN-ERT), which were trained exclusively using
630 historical data, were then applied under these future conditions. Crucially, the method
631 structures and hyperparameters remained fixed, and no retraining was performed; only
632 the historical Tem and Pre values were replaced with their future projections. This
633 approach allows the response of the established historical relationships to new, out-of-
634 sample climatic inputs to be tested. The simulated peak discharges for this analysis were
635 derived from the same three flood events used in the calibration and validation of the
636 Top-SSF model. This experimental design is critical as it isolates the impact of the
637 changed model parameters from the compounding effect of a different future rainfall
638 event. Consequently, any observed change in the simulated flood peak is attributable
639 solely to the sensitivity of the regionalization method to the shift in climatic descriptors.

640 Cumulative distribution functions (CDFs) were then employed to illustrate the
641 discrepancies between the parameter regionalization simulations and the reference
642 simulations (derived from calibrated model parameters) across the historical and
643 projected future periods for the 80 catchments (Fig.12).

644 A comparative analysis of Fig. 12a and 12b reveals a clear amplification of the
645 absolute differences in predicted flood peaks (quantified as the error in runoff modulus)
646 between the two parameter regionalization methods and the reference Top-SSF model
647 simulations during the transition from the historical period to the projected future period.
648 Specifically, the maximum error in runoff modulus for the GBM4-KNN3 method
649 increased by $68.46 \text{ m}^3 \text{ s}^{-1} \text{ km}^{-2}$ from the historical period to the future period, while the
650 increase for the GBM-KNN-ERT method was a smaller $56.65 \text{ m}^3 \text{ s}^{-1} \text{ km}^{-2}$. These results
651 underscore that parameter regionalization methods are inherently sensitive to changing
652 climatic forcing. However, they also provide compelling evidence that the GBM-KNN-
653 ERT method exhibits superior stability and resilience under climate change,
654 demonstrating its potential for more reliable long-term flood risk assessment in
655 ungauged mountainous regions.

656 Exploring the effects of climate change on parameter regionalization methods
657 provides valuable insights for advancing flood prediction research in prediction in
658 ungauged basins. The enhanced stability demonstrated by the GBM-KNN-ERT
659 ensemble offers a promising direction for developing robust regionalization methods
660 capable of navigating the challenges of a non-stationary climate.



661
662 **Fig.12.** Comparison of flood peak runoff modulus between parameter regionalization and
663 calibrated Top-SSF model results, showing cumulative distribution functions (CDFs) of
664 absolute differences for 80 catchments during (a) historical and (b) future periods.

665 5.5. Uncertainty and limitation

666 The uncertainty in this study arises from several sources, including the
667 hydrological model, the regionalization methods, and the data itself. A critical
668 evaluation of these sources helps to contextualize our findings and assess the
669 generalizability of the ensemble method. Uncertainty from the hydrological model is
670 inherent in its structure and the calibrated parameters. Although the Top-SSF model
671 performed well, its parameters are effective values subject to equifinality. This
672 uncertainty in the "true" parameter values can be viewed as a form of calibration bias,
673 which serves as the target data for our regionalization. To mitigate this, we employed
674 the robust SCE-UA optimization algorithm and focused only on sensitive parameters.
675 Uncertainty is also introduced by the regionalization methods themselves, as the
676 training data derived from donor catchments are susceptible to errors that can impact
677 model performance (Mosavi et al., 2018; Xu et al., 2021).

678 A specific methodological choice was the exclusion of deep learning architectures,
679 such as Multilayer Perceptrons or Long Short-Term Memory (LSTM) networks. This

680 decision was guided by several factors. First, parameter regionalization is a static
681 regression problem, mapping time-invariant catchment descriptors to model parameters,
682 which does not align with the sequential data structure for which LSTM is designed.
683 Second, deep networks typically require large datasets to avoid overfitting; with a
684 dataset of 80 catchments, traditional ML methods like GBM and ERT are often more
685 robust and less prone to memorizing training data. Third, a key advantage of parameter
686 regionalization over purely data-driven forecasting is its potential for physical
687 interpretability. The tree-based models employed offer a degree of transparency,
688 whereas DL models often function as "black boxes", a characteristic contrary to our
689 goal of developing an interpretable tool for water resource management.

690 Furthermore, the primary contribution of this study is not the identification of a
691 single superior algorithm, but the demonstration of a data-driven framework for
692 constructing a locally optimal ensemble. The complementarity of the chosen models
693 was not assumed but empirically validated through a competitive evaluation process.
694 Each of the seven ML methods was independently trained and assessed for its ability to
695 estimate each sensitive parameter. The final GBM-KNN-ERT ensemble was
696 constructed by selecting only the empirically best-performing model for each parameter
697 based on objective metrics (R^2 , RMSE, STD). The very fact that different methods were
698 selected for different hydrological parameters provides direct empirical evidence of
699 their complementary strengths, thus validating the ensemble method.

700 Furthermore, the specific GBM-KNN-ERT combination identified is necessarily
701 data-dependent, raising questions about its transferability. However, this study primary

702 contribution is not the specific model combination itself, but rather the demonstration
703 of a data-driven method for constructing a locally optimal ensemble. This method is
704 designed to be generalizable; applying the same competitive evaluation process to a
705 new region would identify the best ensemble for that specific dataset. The key to
706 overcoming these limitations and ensuring robust generalization lies in genuine model
707 complementarity. The ensemble method's success is not an artifact of overfitting to
708 calibration bias or data quirks. Instead, it stems from a physically plausible "division of
709 labor," where different models are empirically shown to be better suited for
710 regionalizing parameters governed by distinct physical processes. The ensemble
711 method's superior stability in the out-of-sample climate change stress test further
712 supports this conclusion, indicating that it has captured robust underlying relationships,
713 not just noise.

714 To manage methodological uncertainty, we employed K-fold cross-validation to
715 ensure robust performance evaluation and RandomizedSearchCV for hyperparameter
716 tuning to minimize overfitting (Bergstra and Bengio, 2012). A key methodological
717 decision was to evaluate the regionalization methods against the outputs of the
718 calibrated Top-SSF model, rather than directly against observed flood events. This
719 approach was chosen for two primary reasons. First, it isolates the performance of the
720 parameter regionalization itself. The calibrated simulation represents the theoretical
721 'best-case' performance for the given hydrological model structure; consequently, any
722 deviation from this benchmark can be directly attributed to imperfections in the
723 regionalization method, rather than being confounded by the inherent structural

724 limitations of the Top-SSF model. Second, this strategy ensures that the machine
725 learning models learn the underlying physical relationships intended by the
726 hydrological model, not simply mimic data noise or measurement errors present in the
727 observations. If trained against raw observations, the ML methods might derive
728 'spurious' parameter sets that compensate for both the hydrological model's structural
729 flaws and observational errors. Such parameters could appear effective but would lack
730 physical meaning and generalizability. These measures, combined with the evidence
731 for model complementarity, provide a strong basis for the scientific validity and
732 potential for generalization of our proposed ensemble method.

733 **6. Conclusions**

734 This study introduces a novel multi-machine learning ensemble method (GBM-
735 KNN-ERT) to enhance model parameter transferability and improve flood prediction
736 in ungauged mountainous catchments. The proposed GBM-KNN-ERT method
737 demonstrated a substantial advancement in both flood prediction accuracy and model
738 robustness, achieving exceptional performance with 90% of ungauged catchments
739 exhibiting a NSE exceeding 0.9, a significant 67.44% improvement compared to the
740 best single machine learning method evaluated in this study. Importantly, the GBM-
741 KNN-ERT method exhibited remarkable stability under simulated climate change,
742 thereby highlighting its potential for reliable application in non-stationary hydrological
743 environments. Furthermore, the method demonstrated notable adaptability to varying
744 donor-catchment configurations, where an optimal balance between predictive
745 accuracy and computational efficiency with a relatively limited set of 20–40 high-

746 quality donor catchments (NSE >0.85). By integrating the diverse strengths of multiple
747 machine learning with hydrological model, the proposed methodology significantly
748 advances the field of flood prediction in ungauged catchments, offering a reliable tool
749 for water resource management and flood disaster mitigation.

750 **Acknowledgements**

751 This research was supported by the Joint Funds of the National Natural Science
752 Foundation of China (**U2240226**), the National Natural Science Foundation of China
753 (**42271038**) and the National Key Research and Development Program of China
754 (**2022FY100205**).

755 **Competing interests**

756 The authors declare that they have no known competing financial interests or
757 personal relationships that could have appeared to influence the work reported in this
758 paper.

759 **Author contributions**

760 In this study, K L, G W, and J G were responsible for the conceptualization of the
761 research. Data curation was carried out by K L, L G, and X S, while formal analysis
762 was performed by K L, J G, and J M. The methodology was developed by K L, L G, P
763 H, and J L. Project administration was overseen by G W and J G. K L took the lead in
764 writing the original draft, and the writing, review, and editing process involved
765 contributions from K L, G W, J L, P H, J M, X Z, and J G.

766 **Code and data availability**

767 The code used in this study is available upon request from the authors. The

768 meteorological, soil characteristics, and topography datasets are publicly accessible
769 online, as detailed in Table 1. The hourly flood data for the 80 catchments were sourced
770 from China's Hydrological Yearbook. These data are not publicly available due to
771 governmental restrictions but can be accessed by contacting the corresponding author
772 for further information.

773 **References**

774 Arsenault, R., Breton-Dufour, M., Poulin, A., Dallaire, G.Romero-Lopez, R. (2019).
775 Streamflow prediction in ungauged basins: analysis of regionalization methods
776 in a hydrologically heterogeneous region of Mexico. *Hydrological Sciences
777 Journal*, 64(11): 1297-1311. <https://doi.org/10.1080/02626667.2019.1639716>

778 Arsenault, R., Martel, J.Mai, J. (2022). Continuous streamflow prediction in ungauged
779 basins: Long Short-Term Memory Neural Networks clearly outperform
780 hydrological models. *Hydrol. Earth Syst. Sci.* 1-29.
781 <https://doi.org/10.5194/hess-27-139-2023>

782 Bellman, R.E. (1961). On the reduction of dimensionality for classes of dynamic
783 programming processes. RAND Corp., Santa Monica, Calif., Paper P-2243.

784 Bergstra, J.Bengio, Y. (2012). Random search for hyper-parameter optimization.
785 *Journal of machine learning research*, 13(2).

786 Beven, K.J., Kirkby, M.J., Freer, J.E.Lamb, R. (2021). A history of TOPMODEL.
787 *Hydrology and Earth System Sciences*, 25(2): 527-549.
788 <https://doi.org/10.5194/hess-25-527-2021S>

789 Bishop, C.M.Nasrabadi, N.M., (2006). Pattern recognition and machine learning
790 (information science and statistics). New York: Springer-Verlag.

791 Breiman, L. (2001). Random forests. *Machine learning*, 45: 5-32.

792 Cheng, Q., Gao, L., Zuo, X.Zhong, F. (2019). Statistical analyses of spatial and
793 temporal variabilities in total, daytime, and nighttime precipitation indices and
794 of extreme dry/wet association with large-scale circulations of Southwest China,
795 1961–2016. *Atmospheric research*, 219: 166-182.
796 <https://doi.org/10.1109/ACCESS.2018.2886549>

797 Choi, J., Kim, U.Kim, S. (2023). Ecohydrologic model with satellite-based data for
798 predicting streamflow in ungauged basins. *Science of The Total Environment*,
799 903: 166617. <https://doi.org/10.1016/j.scitotenv.2023.166617>

800 Dai, Y., Shangguan, W., Duan, Q., Liu, B., Fu, S.Niu, G. (2013). Development of a
801 China dataset of soil hydraulic parameters using pedotransfer functions for land
802 surface modeling. *Journal of Hydrometeorology*, 14(3): 869-887.
803 <https://doi.org/10.1175/JHM-D-12-0149.1>

804 Dakhlaoui, H., Bargaoui, Z.Bárdossy, A. (2012). Toward a more efficient calibration
805 schema for HBV rainfall–runoff model. *Journal of Hydrology*, 444: 161-179.
806 <https://doi.org/10.1016/j.jhydrol.2012.04.015>

807 Ding, Y.Peng, S. (2020). Spatiotemporal trends and attribution of drought across China
808 from 1901–2100. *Sustainability*, 12(2): 477.
809 <https://doi.org/10.3390/su12020477>

810 Duan, Q., Sorooshian, S.Gupta, V.K. (1994). Optimal use of the SCE-UA global
811 optimization method for calibrating watershed models. *Journal of Hydrology*,
812 158(3): 265-284. [https://doi.org/10.1016/0022-1694\(94\)90057-4](https://doi.org/10.1016/0022-1694(94)90057-4)

813 Friedman, J.H. (2002). Stochastic gradient boosting. *Computational statistics & data*
814 *analysis*, 38(4): 367-378. [https://doi.org/10.1016/S0167-9473\(01\)00065-2](https://doi.org/10.1016/S0167-9473(01)00065-2)

815 Gan, B., Liu, X., Yang, X., Wang, X.Zhou, J. (2018). The impact of human activities on
816 the occurrence of mountain flood hazards: lessons from the 17 August 2015
817 flash flood/debris flow event in Xuyong County, south-western China.
818 *Geomatics, Natural Hazards and Risk*, 9(1): 816-840.
819 <https://doi.org/10.1080/19475705.2018.1480539>

820 Gao, J., Kirkby, M.Holden, J. (2018). The effect of interactions between rainfall
821 patterns and land-cover change on flood peaks in upland peatlands. *Journal of*
822 *Hydrology*, 567: 546-559. <https://doi.org/10.1016/j.jhydrol.2018.10.039>

823 Garambois, P.A., Roux, H., Larnier, K., Labat, D.Dartus, D. (2015). Parameter
824 regionalization for a process-oriented distributed model dedicated to flash
825 floods. *Journal of Hydrology*, 525: 383-399.
826 <https://doi.org/10.1016/j.jhydrol.2015.03.052>

827 Gauch, M., Mai, J.Lin, J. (2021). The proper care and feeding of CAMELS: How
828 limited training data affects streamflow prediction. *Environmental Modelling &*
829 *Software*, 135: 104926. <https://doi.org/10.1016/j.envsoft.2020.104926>

830 Geurts, P., Ernst, D.Wehenkel, L. (2006). Extremely randomized trees. *Machine*
831 *Learning*, 63(1): 3-42. <https://doi.org/10.1007/s10994-006-6226-1>

832 Golian, S., Murphy, C.Meresa, H. (2021). Regionalization of hydrological models for
833 flow estimation in ungauged catchments in Ireland. *Journal of Hydrology: Regional*
834 *Studies*, 36: 100859. <https://doi.org/10.1016/j.ejrh.2021.100859>

835 Guo, L., Huang, K., Wang, G.Lin, S. (2022). Development and evaluation of
836 temperature-induced variable source area runoff generation model. *Journal of*
837 *Hydrology*, 610: 127894. <https://doi.org/10.1016/j.jhydrol.2022.127894>

838 Guo, Y., Zhang, Y., Zhang, L.Wang, Z. (2021). Regionalization of hydrological
839 modeling for predicting streamflow in ungauged catchments: A comprehensive
840 review. *Wiley Interdisciplinary Reviews: Water*, 8(1): e1487.
841 <https://doi.org/10.1002/wat2.1487>

842 Gupta, A.K., Chakraborty, S., Ghosh, S.K.Ganguly, S. (2023). A machine learning
843 model for multi-class classification of quenched and partitioned steel
844 microstructure type by the k-nearest neighbor algorithm. *Computational*
845 *Materials Science*, 228: 112321.
846 <https://doi.org/10.1016/j.commatsci.2023.112321>

847 Hastie, T., Tibshirani, R.Friedman, J., (2009). The elements of statistical learning.
848 Citeseer.

849 Hersbach, H., Bell, B., Berrisford, P., Biavati, G., Horányi, A., Muñoz Sabater, J.,
850 Nicolas, J., Peubey, C., Radu, R., Rozum, I., Schepers, D., Simmons, A., Soci,
851 C., Dee, D.Thépaut, J.-N., (2023). ERA5 hourly data on single levels from 1940
852 to present, Copernicus Climate Change Service (C3S) Climate Data Store
853 (CDS)[Dataset]. <https://doi.org/10.24381/cds.adbb2d47> (Accessed on 08-06-
854 2023)

855 Hua, F., Wang, L., Fisher, B., Zheng, X., Wang, X., Douglas, W.Y., Tang, Y., Zhu,
856 J.Wilcove, D.S. (2018). Tree plantations displacing native forests: The nature
857 and drivers of apparent forest recovery on former croplands in Southwestern
858 China from 2000 to 2015. *Biological Conservation*, 222: 113-124.
859 <https://doi.org/10.1016/j.biocon.2018.03.034>

860 Jordan, M.I.Mitchell, T.M. (2015). Machine learning: Trends, perspectives, and
861 prospects. *Science*, 349(6245): 255-260. <https://doi.org/10.1126/science.aaa841>

862 Jung, Y. (2018). Multiple predicting K-fold cross-validation for model selection.
863 *Journal of Nonparametric Statistics*, 30(1): 197-215.
864 <https://doi.org/10.1080/10485252.2017.1404598>

865 Kanishka, G.Eldho, T. (2017). Watershed classification using isomap technique and
866 hydrometeorological attributes. *Journal of Hydrologic Engineering*, 22(10):
867 04017040. [https://doi.org/10.1061/\(ASCE\)HE.1943-5584.0001562](https://doi.org/10.1061/(ASCE)HE.1943-5584.0001562)

868 Kratzert, F., Klotz, D., Herrnegger, M., Sampson, A.K., Hochreiter, S.Nearing, G.S.
869 (2019). Toward improved predictions in ungauged basins: Exploiting the power
870 of machine learning. *Water Resources Research*, 55(12): 11344-11354.
871 <https://doi.org/10.1029/2019WR026065>

872 Lenhart, T., Eckhardt, K., Fohrer, N.Frede, H.G. (2002). Comparison of two different
873 approaches of sensitivity analysis. *Physics and Chemistry of the Earth, Parts*
874 A/B/C, 27(9): 645-654. [https://doi.org/10.1016/S1474-7065\(02\)00049-9](https://doi.org/10.1016/S1474-7065(02)00049-9)

875 Li, K., Wang, G., Gao, J., Guo, L., Li, J.Guan, M. (2024). The rainfall threshold of
876 forest cover for regulating extreme floods in mountainous catchments. *Catena*,
877 236: 107707. <https://doi.org/10.1016/j.catena.2023.107707>

878 Li, X., Khandelwal, A., Jia, X., Cutler, K., Ghosh, R., Renganathan, A., Xu, S., Tayal,
879 K., Nieber, J.Duffy, C. (2022). Regionalization in a global hydrologic deep
880 learning model: from physical descriptors to random vectors. *Water Resources*
881 *Research*, 58(8): e2021WR031794. <https://doi.org/10.1029/2021WR031794>

882 Li, Z., Xu, X., Yu, B., Xu, C., Liu, M.Wang, K. (2016). Quantifying the impacts of
883 climate and human activities on water and sediment discharge in a karst region
884 of southwest China. *Journal of Hydrology*, 542: 836-849.
885 <https://doi.org/10.1016/j.jhydrol.2016.09.049>

886 Liu, C., Guo, L., Ye, L., Zhang, S., Zhao, Y.Song, T. (2018). A review of advances in
887 China's flash flood early-warning system. *Natural hazards*, 92: 619-634.
888 <https://doi.org/10.1007/s11069-018-3173-7>

889 Luo, P., He, B., Takara, K., Xiong, Y.E., Nover, D., Duan, W.Fukushi, K. (2015).
890 Historical assessment of Chinese and Japanese flood management policies and

891 implications for managing future floods. *Environmental Science & Policy*, 48:
892 265-277. <https://doi.org/10.1016/j.envsci.2014.12.015>

893 McMillan, H.K. (2021). A review of hydrologic signatures and their applications. *Wiley
894 Interdisciplinary Reviews: Water*, 8(1): e1499.
<https://doi.org/10.1002/wat2.1499>

895 Morel-Seytoux, H.J.Khanji, J. (1974). Derivation of an equation of infiltration. *Water
896 Resources Research*, 10(4): 795-800.
<https://doi.org/10.1029/WR010i004p00795>

897 Mosavi, A., Ozturk, P.Chau, K.w. (2018). Flood prediction using machine learning
898 models: Literature review. *Water*, 10(11): 1536.
<https://doi.org/10.3390/w10111536>

899 Nearing, G., Cohen, D., Dube, V., Gauch, M., Gilon, O., Harrigan, S., Hassidim, A.,
900 Klotz, D., Kratzert, F., Metzger, A., Nevo, S., Pappenberger, F., Prudhomme, C.,
901 Shalev, G., Shenzis, S., Tekalign, T.Y., Weitzner, D.Matias, Y. (2024). Global
902 prediction of extreme floods in ungauged watersheds. *Nature*, 627(8004): 559-
903 563. <https://doi.org/10.1038/s41586-024-07145-1>

904 Pachauri, R.K., Allen, M.R., Barros, V.R., Broome, J., Cramer, W., Christ, R., Church,
905 J.A., Clarke, L., Dahe, Q.Dasgupta, P., (2014). Climate change 2014: synthesis
906 report. Contribution of Working Groups I, II and III to the fifth assessment
907 report of the Intergovernmental Panel on Climate Change.

908 Papageorgaki, I.Nalbantis, I. (2016). Classification of Drainage Basins Based on
909 Readily Available Information. *Water Resources Management*, 30(15): 5559-
910 5574. <https://doi.org/10.1007/s11269-016-1410-y>

911 Pugliese, A., Persiano, S., Bagli, S., Mazzoli, P., Parajka, J., Arheimer, B., Capell, R.,
912 Montanari, A., Blöschl, G.Castellarin, A. (2018). A geostatistical data-
913 assimilation technique for enhancing macro-scale rainfall-runoff simulations.
914 *Hydrology and Earth System Sciences*, 22(9): 4633-4648.
<https://doi.org/10.5194/hess-22-4633-2018>

915 Qi, W., Zhang, C., Fu, G.Zhou, H. (2016). Quantifying dynamic sensitivity of
916 optimization algorithm parameters to improve hydrological model calibration.
917 *Journal of Hydrology*, 533: 213-223.
<https://doi.org/10.1016/j.jhydrol.2015.11.052>

918 Ragettli, S., Zhou, J., Wang, H., Liu, C.Guo, L. (2017). Modeling flash floods in
919 ungauged mountain catchments of China: A decision tree learning approach for
920 parameter regionalization. *Journal of Hydrology*, 555: 330-346.
<https://doi.org/10.1016/j.jhydrol.2017.10.031>

921 Rockström, J., Gupta, J., Qin, D., Lade, S.J., Abrams, J.F., Andersen, L.S., Armstrong
922 McKay, D.I., Bai, X., Bala, G., Bunn, S.E., Ciobanu, D., DeClerck, F., Ebi, K.,
923 Gifford, L., Gordon, C., Hasan, S., Kanie, N., Lenton, T.M., Loriani, S.,
924 Liverman, D.M., Mohamed, A., Nakicenovic, N., Obura, D., Ospina, D.,
925 Prodani, K., Rammelt, C., Sakschewski, B., Scholtens, J., Stewart-Koster, B.,
926 Tharammal, T., van Vuuren, D., Verburg, P.H., Winkelmann, R., Zimm, C.,
927 Bennett, E.M., Bringezu, S., Broadgate, W., Green, P.A., Huang, L., Jacobson,
928 L., Ndehedehe, C., Pedde, S., Rocha, J., Scheffer, M., Schulte-Uebbing, L., de
929 45

935 Vries, W., Xiao, C., Xu, C., Xu, X., Zafra-Calvo, N.Zhang, X. (2023). Safe and
936 just Earth system boundaries. *Nature*, 619(7968): 102-111.
937 <https://doi.org/10.1038/s41586-023-06083-8>

938 Sain, S.R. (1996). The Nature of Statistical Learning Theory. *Technometrics*, 38(4):
939 409-409. <https://doi.org/10.1080/00401706.1996.10484565>

940 Salmeron, R., García, C.García, J. (2018). Variance inflation factor and condition
941 number in multiple linear regression. *Journal of statistical computation and*
942 *simulation*, 88(12): 2365-2384.
943 <https://doi.org/10.1080/00949655.2018.1463376>

944 Schoups, G., van de Giesen, N.C.Savenije, H.H.G. (2008). Model complexity control
945 for hydrologic prediction. *Water Resources Research*, 44(12).
946 <https://doi.org/10.1029/2008WR006836>

947 Shangguan, W., Dai, Y., Liu, B., Zhu, A., Duan, Q., Wu, L., Ji, D., Ye, A., Yuan,
948 H.Zhang, Q. (2013). A China data set of soil properties for land surface
949 modeling. *Journal of Advances in Modeling Earth Systems*, 5(2): 212-224.
950 <https://doi.org/10.1002/jame.20026>

951 Song, Z., Xia, J., Wang, G., She, D., Hu, C.Hong, S. (2022). Regionalization of
952 hydrological model parameters using gradient boosting machine. *Hydrology*
953 and *Earth System Sciences*, 26(2): 505-524. <https://doi.org/10.5194/hess-26-505-2022>

955 Tang, S., Sun, F., Liu, W., Wang, H., Feng, Y.Li, Z. (2023). Optimal Postprocessing
956 Strategies With LSTM for Global Streamflow Prediction in Ungauged Basins.
957 *Water Resources Research*, 59(7): e2022WR034352.
958 <https://doi.org/10.1029/2022WR034352>

959 Wainwright, J.Mulligan, M., (2013). Environmental modelling: finding simplicity in
960 complexity. John Wiley & Sons.

961 Wani, O., Beckers, J.V.L., Weerts, A.H.Solomatine, D.P. (2017). Residual uncertainty
962 estimation using instance-based learning with applications to hydrologic
963 forecasting. *Hydrol. Earth Syst. Sci.*, 21(8): 4021-4036.
964 <https://doi.org/10.5194/hess-21-4021-2017>

965 Wu, H., Zhang, J., Bao, Z., Wang, G., Wang, W., Yang, Y.Wang, J. (2022). Runoff
966 modeling in ungauged catchments using machine learning algorithm-based
967 model parameters regionalization methodology. *Engineering*.
968 <https://doi.org/10.1016/j.eng.2021.12.014>

969 Xu, Q., Chen, J., Peart, M.R., Ng, C.-N., Hau, B.C.H.Law, W.W.Y. (2018). Exploration
970 of severities of rainfall and runoff extremes in ungauged catchments: A case
971 study of Lai Chi Wo in Hong Kong, China. *Science of The Total Environment*,
972 634: 640-649. <https://doi.org/10.1016/j.scitotenv.2018.04.024>

973 Xu, T.Liang, F. (2021). Machine learning for hydrologic sciences: An introductory
974 overview. *Wiley Interdisciplinary Reviews: Water*, 8(5).
975 <https://doi.org/10.1002/wat2.1533>

976 Yang, X., Magnusson, J., Rizzi, J.Xu, C.-Y. (2018). Runoff prediction in ungauged
977 catchments in Norway: comparison of regionalization approaches. *Hydrology*
978 *Research*, 49(2): 487-505. <https://doi.org/10.2166/nh.2017.071>

979 Yang, X., Magnusson, J.Xu, C.Y. (2019). Transferability of regionalization methods
980 under changing climate. *Journal of Hydrology*, 568: 67-81.
981 <https://doi.org/10.1016/j.jhydrol.2018.10.030>

982 Zhai, X., Guo, L., Liu, R.Zhang, Y. (2018). Rainfall threshold determination for flash
983 flood warning in mountainous catchments with consideration of antecedent soil
984 moisture and rainfall pattern. *Natural Hazards*, 94: 605-625.
985 <https://doi.org/10.1007/s11069-018-3404-y>

986 Zhang, B., Ouyang, C., Cui, P., Xu, Q., Wang, D., Zhang, F., Li, Z., Fan, L., Lovati, M.,
987 Liu, Y.Zhang, Q. (2024). Deep learning for cross-region streamflow and flood
988 forecasting at a global scale. *The Innovation*, 5(3).
989 <https://doi.org/10.1016/j.xinn.2024.100617>

990 Zhang, Y., Chiew, F.H., Li, M.Post, D. (2018). Predicting runoff signatures using
991 regression and hydrological modeling approaches. *Water Resources Research*,
992 54(10): 7859-7878. <https://doi.org/10.1029/2018WR023325>

993 Zhang, Y., Chiew, F.H., Liu, C., Tang, Q., Xia, J., Tian, J., Kong, D.Li, C. (2020). Can
994 remotely sensed actual evapotranspiration facilitate hydrological prediction in
995 ungauged regions without runoff calibration? *Water Resources Research*, 56(1):
996 e2019WR026236. <https://doi.org/10.1029/2019WR026236>

997 Zhang, Y., Ragettli, S., Molnar, P., Fink, O.Peleg, N. (2022). Generalization of an
998 Encoder-Decoder LSTM model for flood prediction in ungauged catchments.
999 *Journal of Hydrology*, 614: 128577.
1000 <https://doi.org/10.1016/j.jhydrol.2022.128577>

1001 Zounemat-Kermani, M., Batelaan, O., Fadaee, M.Hinkelmann, R. (2021). Ensemble
1002 machine learning paradigms in hydrology: A review. *Journal of Hydrology*, 598:
1003 126266. <https://doi.org/10.1016/j.jhydrol.2021.126266>

1004